01 Apr 2022

Evolution Of High-frequency Instabilities In The Presence Of Azimuthally Compact Crossflow Vortex Pattern Over A Yawed Cone

Meelan Choudhari

Fei Li

Pedro Paredes

Lian Duan
Missouri Unviersity of Science and Technology, duanl@mst.edu

Recommended Citation

M. Choudhari et al., "Evolution Of High-frequency Instabilities In The Presence Of Azimuthally Compact Crossflow Vortex Pattern Over A Yawed Cone," *Theoretical and Computational Fluid Dynamics*, vol. 36, no. 2, pp. 181 - 204, Springer, Apr 2022.
The definitive version is available at https://doi.org/10.1007/s00162-021-00594-8

Theor. Comput. Fluid Dyn. (2022) 36:181–204
https://doi.org/10.1007/s00162-021-00594-8

ORIGINAL ARTICLE

Meelan Choudhari · Fei Li · Pedro Paredes · Lian Duan

Evolution of high-frequency instabilities in the presence of azimuthally compact crossflow vortex pattern over a yawed cone

Received: 19 February 2021 / Accepted: 3 November 2021 / Published online: 6 January 2022

Abstract Hypersonic boundary-layer flows over a circular cone at a moderate yaw angle can support strong crossflow instability away from the windward and leeward rays on the plane of symmetry. Due to the more efficient excitation of stationary crossflow vortices by surface roughness, a possible path to transition in such flows corresponds to rapid amplification of the high-frequency instabilities sustained in the presence of finite amplitude stationary crossflow vortices. This paper presents a computational analysis of crossflow instability over a 7-degree half-angle, yawed circular cone in a Mach 6 free stream. Specifically, the nonlinear evolution of an azimuthally localized crossflow vortex pattern and the linear amplification characteristics of high-frequency instabilities evolving in the presence of that pattern are described for the first time. Focusing on the azimuthally compact vortex pattern allows us to overcome significant limitations of the prior secondary instability analyses of azimuthally inhomogeneous boundary layer flows. A comparison between plane-marching parabolized stability equations and direct numerical simulations (DNS) reveals favorable agreement in regard to mode shapes, most amplified disturbance frequencies, and the N-factor evolution. In contrast, the quasiparallel predictions are found to result in a severe underprediction of the N-factors. The most amplified high-frequency instabilities are found to originate from Mack's second mode waves sustained within the upstream region of nearly unperturbed, quasi-homogeneous boundary layer.

Keywords Laminar-turbulent transition · Hypersonic boundary layers · Crossflow instability · Second mode instability · Secondary instability · Yawed cone

1 Introduction

Boundary-layer transition from the laminar to a turbulent state is known to have a major impact on the design and performance of hypersonic flight vehicles. When the vehicle surface is relatively smooth, the transition process is initiated by linear instabilities of the laminar boundary layer, including Mack's second mode instability, Görtler instabilities, stationary and traveling modes of crossflow instability, and the attachment line instability [1–3].

Communicated by Sergio Pirozzoli.

M. Choudhari (✉) · F. Li
NASA Langley Research Center, Hampton, VA 23681, USA
E-mail: m.m.choudhari@nasa.gov

P. Paredes
National Institute of Aerospace, Hampton, VA 23666, USA

L. Duan
The Ohio State University, Columbus, OH 43210, USA

Regardless of the speed regime, linear stability correlations based on the primary instability mechanisms have been reasonably successful in predicting the onset of boundary-layer transition when a single instability mechanism dominates the transition process. However, in recent years, the limitations of this approach have also become increasingly apparent in the case of crossflow-dominated transition in three-dimensional (3D) boundary layers. Because the boundary-layer flows encountered in a majority of technological applications are 3D in nature, accurate prediction of crossflow transition has significant practical implications. Measurements of crossflow instability in low-speed 3D boundary layers have shown that the onset of transition occurs only after the primary crossflow instabilities have reached substantially large amplitudes so that appreciable portions of the pretransitional boundary layer involve finite amplitude crossflow modes that evolve much more slowly in comparison with the predictions of the linear stability theory [3,4]. The slow variation in the amplitude of the quasisaturated crossflow modes also implies that an absolute amplitude criterion based on nonlinear predictions of the primary crossflow instability would not be a robust predictor of the transition location [4]. The onset of transition in the presence of finite amplitude stationary crossflow vortices is usually initiated by the rapid growth of secondary instabilities, and the measured transition locations in a low-speed, infinite-span swept wing boundary layer have been found to correlate well with the linear growth correlations based on the amplification of those secondary instability waves [4].

Even though the basic physics of the stationary crossflow instability remains the same at higher Mach numbers, predictions of crossflow transition over high-speed configurations must tackle an additional source of complexity. Whereas low-speed configurations such as the high aspect ratio wings of a subsonic transport aircraft involve boundary-layer flows that are nearly homogeneous in the spanwise direction, the geometry of most supersonic and hypersonic flight vehicles corresponds to a relatively slender configuration with an O(1) or lower aspect ratio. Thus, the azimuthal inhomogeneity of the 3D boundary-layer flow must be taken into consideration in predicting the evolution of the crossflow instabilities.

For boundary-layer flows that are homogeneous in at least one spatial dimension, such as the flow past an axisymmetric body at zero angle of attack or a 2D/infinite-swept wing, the growth of linear perturbations can be easily analyzed by invoking a Fourier ansatz in the homogeneous coordinate. A majority of boundary-layer flows encountered in practical applications are fully three dimensional in nature, i.e., vary along both coordinate directions parallel to the body surface. The boundary-layer flows over a yawed circular cone and an elliptic cone represent canonical examples of such flows. The lack of flow homogeneity along either the streamwise or the azimuthal direction results in both fundamental and practical challenges for linear stability theory and its application to transition prediction. In particular, the modal ansatz for the perturbation field, which decouples the various length scales (i.e., Fourier modes) along the azimuthal flow direction, is no longer applicable in the case of such fully three-dimensional boundary layers. Even though a local modal ansatz may be justified under the framework of classical stability theory for weakly nonparallel mean flows, the fact that disturbance amplitudes evolve in both directions parameterizing the body surface makes it necessary to invoke additional (and typically ad hoc) approximations to select a curvilinear trajectory for the integration of disturbance amplification rates. These difficulties are further amplified in computing the nonlinear evolution of primary instabilities and the ensuing growth of secondary perturbations.

The canonical high-speed configuration of a circular cone at nonzero yaw (or, equivalently, at a nonzero angle of incidence) includes the necessary elements to study both crossflow development and mixed mode transition in the context of both supersonic [4–12] and hypersonic [13–35] boundary-layer flows. Control of crossflow transition via patterned roughness has been investigated via wind tunnel experiments in Refs. [36,37]. Instability mechanisms for the boundary-layer flow over an elliptic cone have also been investigated in Refs. [20,38–56]. While the elliptic cone configuration supports similar instability mechanisms as the circular cone at an angle of incidence, the details of the transition patterns can be rather different as noted by Berger et al. [45].

Recent experimental measurements have established the presence of both stationary and traveling modes of crossflow instability in 3D hypersonic boundary layers over cones. Oil flow visualizations [4] and surface heat transfer measurements have revealed the relatively strong, axially elongated vorticity structures associated with stationary crossflow instability. Measurements of unsteady surface pressure on an elliptic cone [51] have yielded encouraging comparisons with the predictions of traveling crossflow instability by Li et al. [20]. Measurements of crossflow instability over a yawed circular cone in three different Mach 6 wind tunnels have been reported in Refs. [21–26]. Besides a low-frequency peak between 15 and 60 kHz that was likely to have been caused by traveling crossflow disturbances, the circular cone measurements from Refs. [21–24] indicated higher-frequency peaks, particularly in the vicinity of 300 to 350 kHz. However, a lack of sufficient detail in the measurements prevented them from establishing whether these disturbances were associated with

Mack's second mode instabilities in the underlying boundary layer over the yawed cone, or with the secondary instabilities of finite amplitude crossflow instabilities in that boundary layer. Measurements by Craig and Saric [25,26] revealed lower-frequency disturbances near 110 kHz, i.e., at higher frequencies than those of the traveling crossflow disturbances of the unperturbed boundary layer.

Computations of secondary instability of crossflow modes in a hypersonic boundary layer were first reported by Li et al. [30] for the case of a quasiperiodic, i.e., noncompact pattern of stationary crossflow vortices that was computed by using direct numerical simulations. The predicted high-frequency secondary instabilities with the highest growth rates had frequencies that were comparable to those measured in the experiments at the Technical University of Braunschweig [21] and the Purdue University [22–24,34], but the computations had also revealed the existence of less unstable modes with lower disturbance frequencies that were comparable to those measured by Craig and Saric [26]. Recently, more detailed secondary instability analyses for large-amplitude stationary crossflow vortices over the yawed cone were described by Li et al. [30–32] and Moyes et al. [33]. These works have identified three major types of instability modes: those that originate from low-frequency traveling crossflow modes and high-frequency Mack mode instabilities of the unperturbed boundary layer, but get modulated (and potentially further destabilized) by the presence of large-amplitude stationary crossflow vortices; and genuine, high-frequency secondary instability modes that arise entirely due to the presence of large-amplitude stationary crossflow vortices and are concentrated in the shear layer that bounds those vortices. Secondary instabilities of crossflow vortices over the simpler configuration of a spanwise homogeneous swept wing boundary layer at Mach 6 have been reported by Xu et al. [57,58], who identified the role of the so called Type II secondary instability modes.

Li et al. [30] focused on the secondary instability of selected individual vortices from the crossflow vortex pattern excited via an azimuthally periodic array of roughness elements upstream. Even though the disturbance source was azimuthally periodic, the resulting vortex pattern was strongly modulated in the azimuthal direction, with the strongest vortices located within the leeward half of the cone. To enable an application of the secondary instability theory, each crossflow vortex of interest was rendered azimuthally periodic via detrending and Fourier low-pass filtering. Thus, the cumulative effects of the azimuthal nonuniformity of the vortex pattern are neglected in this analysis. In the present work, we build upon the prior research by Li et al. [30–32] by addressing the other limiting case of a compact disturbance source, which leads to a commensurately compact crossflow vortex pattern behind the source. Specifically, this paper is devoted to the computations of azimuthally compact, stationary crossflow vortex packets over a 7-degree half-angle, yawed circular cone in a Mach 6 free stream, namely, stationary crossflow vortex patterns generated by azimuthally localized roughness height distributions and the characteristics of high-frequency secondary instabilities associated with those crossflow vortex packets. Such analysis is important for both predicting and controlling the process of laminar-turbulent transition over the cone, since roughness elements provide a potential means to control the transition process initiated by stationary crossflow vortices.

By analyzing the secondary instability of the entire vortex pattern, we are able to avoid the ad hoc approximation associated with local periodicity and, hence, provide an exact account of the interactions between secondary instability perturbations across neighboring vortices. It is worth emphasizing that while the modulation of the noncompact vortex pattern in the work by Li et al. [30–32] was caused by the basic state inhomogeneity, the modulated vortex patterns encountered in practice would likely reflect a combined effect of the inhomogeneity of both the basic state and the forcing field as studied herein. Similar to Li et al. [30–32], the present paper targets the high-frequency secondary instabilities, including the modes that originate from the Mack mode instability as well as those that emerge from the otherwise stable part of the spectrum after the stationary vortices have attained sufficiently large amplitudes. We address the effects of the crossflow vortex modulation on the secondary instability via nonparallel predictions for the evolution of secondary instabilities in the azimuthally inhomogeneous, three-dimensional boundary layer and a comparison between those predictions and the DNS results. Related work may also be found in the earlier references [59,60]. In this context, we also note that the effects of spanwise modulation of stationary crossflow vortices by a subharmonic stationary mode were examined by Choudhari et al. [61] for a subsonic boundary layer over a swept airfoil. They showed that even a weak modulation by the first subharmonic of the input stationary mode leads to a mode splitting phenomenon that leads to a pair of secondary modes with somewhat different amplification rates and that are concentrated within different individual vortex structures across the subharmonic wavelength. A somewhat similar behavior is found in the present context as well.

The remaining sections of this paper are laid out as follows. A brief summary of the flow configuration of interest is given in Sect. 2, which also describes the analysis codes used in this study. The generation of stationary crossflow vortices via selected azimuthal distributions of roughness elements and the subsequent evolution of

the generated vortices is considered in Sect. 3. Development of the secondary instabilities sustained by finite amplitude, stationary crossflow vortices is outlined in Sect. 4 which also includes a comparison between the DNS results and the predictions of parabolized stability equations (PSE). Summary and concluding remarks are presented in Sect. 5.

2 Flow configuration and analysis codes

The flow configuration of interest corresponds to a yawed circular cone in a uniform, hypersonic free stream (Fig. 1). The primary configuration for the Purdue experiments corresponds to a 0.457 meter (18 inch) long, nominally sharp nosed cone (modeled with a nose radius of 10^{-4} times the cone length) with a half angle of 7 degrees and a yaw angle, α, equal to 6 degrees. The freestream conditions correspond to a free-stream Mach number of $M_\infty = 6$, unit Reynolds number $Re = 10.8 \times 10^6$ per meter, and free-stream temperature $T_\infty = 52.44$ K. The freestream velocity at these conditions corresponds to $U_\infty = 870.9$ m/s. The temperature of the model surface, T_w, is equal to 300 K. The above flow configuration is identical to that used by Li et al. [30,31] and the same computational mesh and basic state solution from those studies are used in the present work as well. For the sake of completeness, the details of the computational scheme are repeated below.

The working fluid is assumed to be perfect gas (air) and the usual constitutive relations for a Newtonian fluid are used: the viscous stress tensor is linearly related to the rate-of-strain tensor, and the heat flux vector is linearly related to the temperature gradient through Fourier's law. The coefficient of viscosity is computed from Sutherland's law, and the coefficient of thermal conductivity is computed by assuming a constant Prandtl number Pr = 0.71. The unperturbed boundary-layer flow over the cone is computed using the VULCAN-CFD (Viscous Upwind aLgorithm for Complex flow ANalysis) software [62]. The code solves the unsteady, conservation equations appropriate for laminar or turbulent flow of calorically or thermally perfect gases with a spatially second-order accurate cell-centered finite volume scheme. In the present computations, the inviscid fluxes were constructed using the MUSCL $\kappa = 0$ scheme, the van Albada gradient limiter [63], and the low dissipation flux split scheme (LDFSS) of Edwards [64,65]. The cell face gradients required to construct the viscous fluxes were obtained using an auxiliary control volume approach that results in a compact viscous stencil that produces a second-order accurate approximation of the full Navier–Stokes viscous fluxes. In previous work, similar computations of the mean flow over an elliptic cone configuration were cross-validated against the solutions obtained with the LAURA code [66] for various grid sizes [18]. Additional grid sensitivity analysis for the present flow configuration is reported by Li et al. [31].

The evolution of stationary crossflow disturbances in the boundary-layer flow is computed by using the basic state obtained from the VULCAN solution described above. The stationary crossflow vortices are excited via an array of axially localized roughness elements centered at $X = 0.18$ m. The streamwise shape of the roughness elements corresponds to a half-wavelength cosine shape with an axial wavelength of 0.008 m and a peak height perturbation of 5μ m. Different azimuthal distributions of roughness height are used, including an azimuthally periodic forcing with a single azimuthal wavenumber of $n = 60$ (where n denotes the number of vortex wavelengths across the full circumference of the circular cone) and various localized azimuthal distributions obtained by windowing the periodic distribution over one half wavelength, one wavelength, three wavelengths, and five wavelengths, respectively. The choice of roughness parameters used herein enables one to approximate the observed spacing and the strength of nonlinear crossflow vortices as gauged by the rollup of mass-flux contours across the cross section and the spatial region (axial and azimuthal locations) of vortices with sufficiently large amplitudes. Given this limited purpose of the roughness array, we invoke the assumption of a

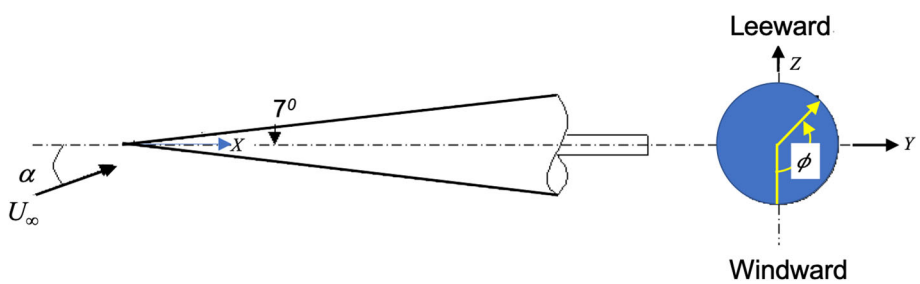

Fig. 1 Schematic of the yawed circular cone (left: top view, right: rear view)

suitably small roughness height to transfer the boundary condition from the actual geometry of the roughness elements to the underlying smooth surface. This amounts to imposing nonzero velocity perturbations and a modified surface temperature based on a linear Taylor series approximation to the unperturbed (i.e., smooth surface) boundary-layer profiles, allowing the no slip condition on the rough surface to be satisfied to the leading order in the regular perturbation approximation [67].

The stationary crossflow disturbances are computed by using a high- order discretization that will be referred to as the DNS solution for simplicity. A detailed description of the governing equations and their numerical solution via the DNS code is given by Wu et al. [68]. The inviscid fluxes from the governing equations are computed using a seventh-order weighted essentially nonoscillatory finite-difference WENO scheme introduced by Jiang and Shu [69], with the WENO adaptation turned off for optimal resolution of the high-frequency secondary instabilities. Both an absolute limiter on the WENO smoothness measurement and a relative limiter on the total variation are employed simultaneously during the simulation. The viscous fluxes are discretized using a fourth-order central difference scheme, and time integration is performed using a third-order low-storage Runge–Kutta scheme [70]. The numerical code has been previously applied to simulation of turbulence in hypersonic boundary layers [71,72] as well as laminar-turbulent transition due to crossflow instability in swept wing boundary layers [73,74]. The lessons learned from these simulations were applied to develop the computational grid for stationary crossflow evolution in the present work.

The primary instability computation is performed on a grid consisting of $600 \times 1200 \times 140$ points in the axial (X), azimuthal (φ), and wall-normal (Y) directions, respectively. Without any loss of generality, the stationary crossflow disturbances are assumed to be symmetric about the windward and leeward planes, so that only one half of the circular cone was included in the computational domain. The grid points are spaced uniformly in the azimuthal direction. For select cases, the numerical accuracy of the basic state calculation was verified by Li et al. [30–32] via computations on a finer grid with significantly higher resolution in the azimuthal and radial directions. Additional calculations for similar configurations had also established that the grid spacing in the axial direction is adequate for the purpose of computing the evolution of the crossflow vortices.

Choudhari et al. [59] had investigated the secondary instability of the finite amplitude stationary crossflow vortices emanating from an azimuthally compact source. They reported quasiparallel, spatial predictions that were based on a planar eigenvalue analysis as first described by Li and Choudhari [75,76] for the case of a periodic pattern of crossflow vortices in infinite-span swept wing boundary layers. For an azimuthally periodic source that leads to a quasiperiodic pattern of crossflow vortices in the downstream region, Li et al. [30,31] had employed both quasiparallel predictions and a nonparallel framework based on plane marching parabolized stability equations (PSE) as described by Paredes et al. [77–79]. For cases involving a quasiperiodic vortex behavior (which applies both when a periodic roughness array extends around the entire circumference of the cone and to the vortex/vortices near the center of a sufficiently wide vortex pattern in cases where the periodic roughness array is truncated to a noncompact azimuthal width), the basic state for each individual vortex can be made azimuthally periodic via a combination of detrending and Fourier low-pass filtering and then used for local secondary instability computations. For further details of the procedure used for secondary instability analysis in this case, the reader is referred to the earlier works by Li et al. [30–32]. In the opposite limiting case that corresponds to a sufficiently compact vortex pattern (i.e., where the entire pattern is limited to a small number of vortices that are nearly parallel to each other), the basic state for secondary instability must include the entire pattern at a given axial location. To set the stage for the stability results presented in Section IV, we now provide a summary of the methodology used to predict the disturbance evolution characteristics.

The secondary instability of the compact vortex pattern due to the single-wavelength forcing is studied with the local, quasiparallel spatial eigenvalue problem (EVP) analysis and the nonparallel plane-marching parabolized stability equations (PSE). The vector of fluid variables, $\mathbf{q} = (\rho, u, v, w, T)^T$, is decomposed into

$$\mathbf{q}(x, y, z, t) = \bar{\mathbf{q}}(x, y, z) + \tilde{\mathbf{q}}(x, y, z, t), \tag{1}$$

where $\bar{\mathbf{q}} = (\bar{\rho}, \bar{u}, \bar{v}, \bar{w}, \bar{T})^T$ is the vector of basic state variables and $\tilde{\mathbf{q}} = (\tilde{\rho}, \tilde{u}, \tilde{v}, \tilde{w}, \tilde{T})^T$ is the vector of perturbation variables. The coordinates (x, y, z) denote a curvilinear, orthogonal, body-fitted coordinate system, where x denotes the distance along the cone meridian at a fixed azimuthal angle φ, y denotes the wall-normal distance from the cone surface, and z represents the azimuthal direction.

In the context of the local, quasiparallel eigenvalue problem (EVP), the basic state and perturbation variables are assumed to be locally independent of x. Therefore, the perturbations are assumed to have the form

$$\tilde{\mathbf{q}}(x, y, z, t) = \hat{\mathbf{q}}(y, z)\exp[\mathrm{i}(\alpha x - \omega t)], \tag{2}$$

where $\omega = 2\pi f$ is the circular frequency, f is the frequency of the perturbation, and α is the complex streamwise wavenumber, with its real part denotes as $\alpha_r = 2\pi/\lambda_x$ and the imaginary part is $\alpha_i = -\sigma$, where λ_x is the local streamwise wavelength of the disturbance and σ is the local growth rate of the perturbation. Substituting Eq. (3) into the linearized Navier–Stokes equations, a generalized EVP is obtained that is quadratic in the eigenvalue α. The companion matrix method can be used to reduce the quadratic terms in α and obtain the linear EVP,

$$A\widehat{q^+} = \alpha B\widehat{q^+}, \tag{3}$$

where $\widehat{q^+} = (\rho, u, v, w, T, \alpha u, \alpha v, \alpha w, \alpha T)^T$. The generalized EVP is solved either with the Arnoldi algorithm combined with a shift-and-invert strategy to calculate a number of eigenvalues on the vicinity of a selected complex value [80,81], or to compute a single eigenvalue with the inverse Rayleigh iteration method [82].

The nonparallel effects are considered in the plane-marching PSE by using the following ansatz for the perturbation field

$$\tilde{\mathbf{q}}(x, y, z, t) = \hat{\mathbf{q}}(x, y, z) \exp\left[\mathrm{i}\left(\int \alpha\left(x^*\right) \mathrm{d}x^* - \omega t\right)\right] \tag{4}$$

where the unknown, streamwise varying wavenumber $\alpha(x)$ is determined in the course of the solution by imposing an additional constraint

$$\int_z \int_y \hat{q}^H \frac{\partial \hat{q}}{\partial \mathrm{x}} \mathrm{d}y\, \mathrm{d}z, \tag{5}$$

which implies a slow variation of the amplitude functions in the streamwise direction in comparison with the phase term. Substituting Eq. (3) into the linearized Navier–Stokes equations and involving the scale separation to neglect the viscous, streamwise derivate terms, the plane-marching PSE are obtained and can be written in the following form

$$\left(\mathbf{L} + \mathbf{M}\frac{\partial}{\partial x}\right)\widehat{\mathbf{q}} = 0 \tag{6}$$

The parabolic system of partial differential equations (6) is solved by marching along the streamwise direction together with the normalization condition of Eq. (5). The initial condition $\widehat{\mathbf{q}}_0 = \hat{\mathbf{q}}(x_0, y, z)$ and $\alpha_0 = \alpha(x_0)$ is given by the quasiparallel EVP solution at the streamwise location x_0 that corresponds to the location just upstream of the neutral location of the selected mode. The Arnoldi algorithm is used to select the mode at an unstable location, and the inverse Rayleigh iteration method is used to calculate the instability mode at the consecutive upstream locations until the mode becomes stable. The PSE marching is initiated near the lower branch neutral location by using an initial disturbance profile obtained from the EVP analysis. A more detailed description of the EVP and the plane-marching PSE methodologies is given in Refs. [77–79].

The disturbance amplification is estimated using the logarithmic amplification ratio, also known as the N-factor, relative to the lower neutral location x_{lb} at which the disturbance first becomes unstable. Thus,

$$N_q(\omega) = -\int_{x_{lb}}^{x} \alpha_i\left(x^*, \omega\right) dx^* + \ln\left[\hat{q}(x)/\hat{q}(x_{lb})\right], \tag{7}$$

where $\hat{q}$ represents an amplitude norm of the disturbance at a given streamwise station, e.g., either the square root of the disturbance kinetic energy integrated in the wall-normal direction or the local maximum of the streamwise velocity fluctuation associated with a given disturbance. The disturbance kinetic energy is defined as

$$\widehat{\mathrm{ke}} = \int_y \rho\left(\hat{u}^H\hat{u} + \hat{v}^H\hat{u} + \hat{w}^H\hat{w}\right) dy. \tag{8}$$

The metric factors associated with the streamwise and azimuthal curvatures are defined as $\mathrm{h_X} = 1 + \kappa \mathrm{y}$ and $h_z = r_b + y\cos(\theta)$, where κ denotes the streamwise curvature, r_b is the local radius and ϑ is the local half-angle along the axisymmetric surface, i.e., $\sin(\theta) = dr_b/dx$. A three-dimensional coordinate transformation of the form $\xi = \xi(x)$, $\eta = \eta(x, y, z)$, and $\zeta = \zeta(x, y, z)$ is used to account for the boundary-layer growth and the curvilinear vortex trajectory, where $\partial\left(\bar{\mathbf{q}}, \tilde{\mathbf{q}}\right)/\partial\xi \ll \partial\left(\bar{\mathbf{q}}, \tilde{\mathbf{q}}\right)/\partial\eta, \partial\left(\bar{\mathbf{q}}, \tilde{\mathbf{q}}\right)/\partial\zeta$. The discretization plane is kept perpendicular to the streamwise direction with $\xi = x$. A fixed domain extent of $[0, \eta_\infty]$, as well as a fixed grid distribution along the η axis is used at all streamwise stations. The semi-infinite domain in η is truncated to

$\eta = [0, \eta_\infty]$, and the grid is clustered toward the wall by using the following one-dimensional transformation from the uniformly spaced finite-difference grid $\eta_0 \in [-1, 1]$ to the grid distribution across η,

$$\eta = l\frac{1-\eta_0}{1+s+\eta_0}, \quad s = 2l/\eta_\infty, \quad l = \frac{\eta_\infty \eta_h}{\eta_\infty - 2\eta_h},$$

where one half of the total number of wall normal grid points are included within $\eta = [0, \eta_h]$. The mapping $y(\xi) = \eta\sqrt{\xi/\xi_0}$ allows the grid extent along the physical y coordinate to expand with the boundary layer growth in the downstream direction. The domain along the ζ axis has a constant extent, but the physical domain extent in z is adjusted with the width of the vortex to ensure that is large enough to capture the secondary instability modes at all streamwise locations. A uniform grid distribution is used across the domain; however, whereas the ζ grid remains fixed at all streamwise locations, the domain along the physical z coordinate is shifted with increasing ξ in order to follow the trajectory of the vortex:

$$\mathrm{z}(\xi) = \mathrm{l}_v\zeta + \int_{\xi_0}^{\xi} \tan(\vartheta(\xi))\, \mathrm{d}\xi, \tag{9}$$

where l_v denotes the vortex width and $\vartheta(\xi)$ denotes the local angle of the vortex trajectory with respect to x.

It may be noted that the derivative matrix operators in the PSE are calculated using the three-dimensional coordinate transformation as explained by Paredes [77]. For example, the derivatives with respect to the streamwise direction x include the transformation terms,

$$\frac{\partial\tilde{\mathbf{q}}}{\partial x} = \frac{\partial\tilde{\mathbf{q}}}{\partial\xi} + \eta_x\frac{\partial\tilde{\mathbf{q}}}{\partial\eta} + \zeta_x\frac{\partial\tilde{\mathbf{q}}}{\partial\zeta},$$

and, given the separation of scales invoked in the PSE approximation, the ξ derivative can be expressed as

$$\frac{\partial\tilde{\mathbf{q}}}{\partial\xi} = \frac{\partial\tilde{\mathbf{q}}}{\partial\xi} + \mathrm{i}\alpha\hat{\mathbf{q}}$$

We end this section with an outline of the procedure used for the DNS of nonstationary instabilities supported by the compact pattern of crossflow vortices. The stationary crossflow vortices excited via the surface deformations represent convective instabilities and, therefore, a separate simulation involving an additional, unsteady forcing is necessary to study the evolution of those nonstationary instabilities in the presence of the finite amplitude, stationary crossflow vortices. Since the boundary-layer flow modified by the crossflow vortices already includes short-scale azimuthal variations, the secondary instabilities can be excited by using an unsteady surface forcing that is invariant along the azimuthal direction, but is localized within a narrow streamwise slot that is centered at $X_0 = 0.28$ m. The time dependence of the wall-forcing function includes a superposition of time harmonic signals comprised of multiple discrete frequencies from 20 kHz to 480 kHz at an interval of 20 kHz. In particular, the forcing distribution corresponds to a nonzero surface-normal velocity of

$$\frac{v'(X,\phi,t)}{U_\infty} = g(X)\sum\nolimits_{j=l}^{n_f} A_j \sin\left(2\pi f_j t\right) \tag{10}$$

at the cone surface, where $f_j = 20 \times j$ kHz and $n_f = 24$. The range of forcing frequencies is guided by the earlier analysis by Li et al. [30–32] as well as by the results of local stability analysis presented in Section IV. The streamwise distribution function $g(X)$ involves the single-wavelength cosine variation, $g(X) = 0.5[1 + cos(2\pi(X - X_0)/w)]$, where the slot width w is set equal to 1 mm. To reduce the computational cost, the unsteady forcing location of $X_0 = 0.28$ m is chosen to be somewhat downstream of the roughness elements used to excite the stationary crossflow vortices. Given the large range of excitation frequencies, the slot width is chosen to be sufficiently narrow so as to excite unsteady disturbances across a broad band of wavenumbers that would couple into the unstable modes at the relevant frequencies. To investigate the linear amplification of the secondary instabilities, a suitably small amplitude of the wall forcing is used, with $A_j = 10^{-7}$ for all j. Fourier decomposition of the time history from the output signal is used to analyze the disturbance evolution at each selected frequency.

Finally, we note that white noise could have been used to define the temporal variation of the forcing function; however, the purpose of this investigation was to study the amplification characteristics of secondary instabilities in the frequency domain and that task is more efficiently accomplished by using the time harmonic

forcing involving a mix of discrete frequencies. A white noise forcing would have required data accumulation over a significantly longer time interval in order to allow accurate Fourier analysis of the data, whereas clean predictions of spectral amplitudes can be obtained by using time harmonic forcing and by accumulating the flow response over a single period of the lowest frequency. For instance, spectral analysis at frequencies from 120 kHz to 480 kHz in intervals of 40 kHz would only require the storage of simulation data over a single period of 40 kHz.

3 Effect of azimuthal extent of roughness distribution on the crossflow vortex pattern

Computational results pertaining to stationary crossflow vortices in the boundary-layer flow over the cone are presented in this section. As mentioned previously, the evolution of the quasiperiodic pattern of stationary crossflow vortices due to an azimuthally periodic array of roughness elements was described by Li et al. [32]. Vortex patterns due to azimuthally compact distributions of roughness elements were first investigated by Choudhari et al. [59]. The present paper includes a broader range of roughness configurations that help bridge the gap between the limiting cases of azimuthally periodic and azimuthally compact forcing, respectively.

The periodic forcing case corresponds to a forcing wavenumber of $n = 60$. The latter wavenumber was chosen to approximate the azimuthal wavelength of the crossflow modes found in the experiments of Craig and Saric [26]. Farther downstream from the forcing location, the vortex structures, or equivalently, streaks generated by the roughness pattern move toward the leeward ray and the streak spacing changes as a result of the nonparallel-flow effects. Consequently, there is a pronounced difference between the larger vortex wavelength near the sideline ray and the smaller wavelength on the leeward side.

The effect of the azimuthal extent of the roughness height distribution on the generated vortex patterns is shown in Fig. 2, which shows the axial velocity contours at $X = 0.4$ m for various selected roughness element distributions. Figure 2a corresponds to the periodic forcing case [32], whereas Figs. 2d, e correspond to azimuthally compact forcing where the periodic forcing is truncated to a single azimuthal wavelength and one half of the azimuthal wavelength, respectively. The half-wavelength azimuthal distribution resembles a single protuberance, whereas the single-wavelength distribution involves a protuberance and a dimple adjacent to each other. Crossflow vortex patterns due to roughness distributions with intermediate azimuthal extents equal to five and three azimuthal wavelengths are plotted in Figs. 2d, c, respectively.

As expected, the localized distributions generate considerably narrower crossflow vortex patterns (Fig. 2b, e) compared to the vortex pattern due to an azimuthally periodic roughness distribution (Fig. 2a). Whereas Fig. 2a for the periodic-forcing case displays at least 12 vortex structures, only three prominent vortex structures are observed for the most compact roughness distributions in Figs. 2d, e. The azimuthal location of roughness elements in the latter two cases was chosen such that the three dominant vortices excited by the azimuthally localized roughness elements are approximately aligned with vortices 8 through 10 from the vortex pattern excited by the periodic roughness height distribution as described in Ref. [32]. The location of vortex 10 from the periodic roughness case is labeled as V10 in Fig. 2a, and for reference, it is also indicated in the remaining parts of Fig. 2. For each of the roughness configurations considered in Fig. 2, the velocity contours associated with the dominant vortices exhibit strong roll-up as reflected in the overturned contours at $X = 0.4$ m, indicating a highly nonlinear crossflow disturbance field at that location. As the roughness pattern becomes increasingly compact, the number of clearly visible vortices within the overall pattern decreases in a monotonic fashion, from nearly 12 in the periodic case (Fig. 2a) to eight for five-wavelength forcing, six for three-wavelength forcing, four in the single-wavelength case, to three in the half-wavelength case (Fig. 2e). As the azimuthal extent of the forcing is increased beyond the last configuration, the case of three-wavelength forcing is the first to indicate the emergence of an apparently quasiperiodic behavior for the center vortices (Fig. 2c) and the quasiperiodic nature extends to increasing number of vortices for the five-wavelength forcing (Fig. 2b) and the periodic roughness array (Fig. 2a), respectively. The similarity of the dominant vortex evolution in the three-wavelength and five-wavelength cases with that in the periodic-forcing case would become more apparent from the subsequent comparison between the vortex amplitudes. Given the relatively smaller number of vortices contained within the vortex patterns in Fig. 2d, e as well as the stronger inhomogeneity across those patterns, those two cases will be referred to as the compact vortex patterns in this paper, and the stability characteristics of these compact vortex patterns will be the primary focus in this work.

A more sensitive detection scheme for the vortex structures excited by the various roughness configurations is based on an automated analysis of the azimuthal distribution of the surface heat flux distribution. Any perturbation quantity associated with a small-amplitude stationary crossflow disturbance has a quasi-periodic

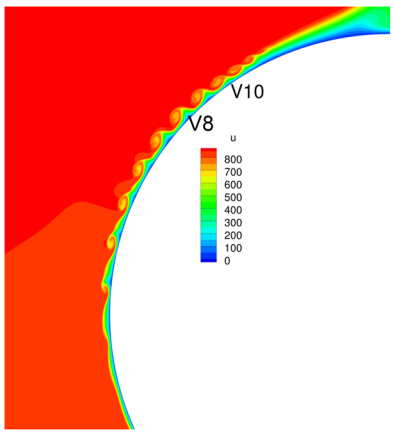

(a) Periodic forcing

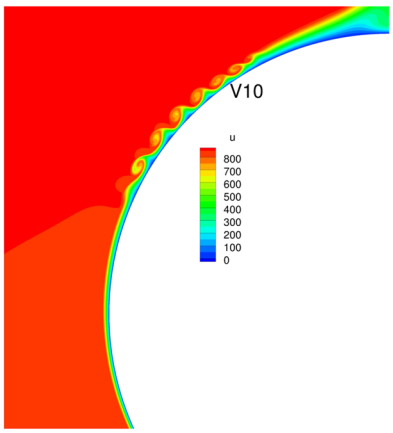

(b) 5-wavelength forcing

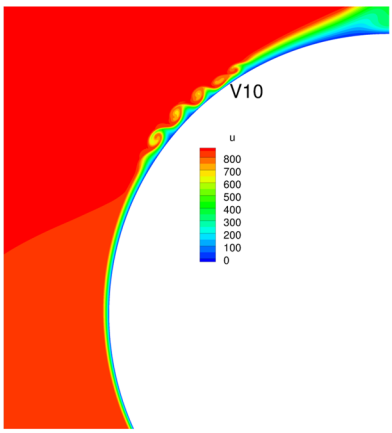

(c) 3-wavelength forcing

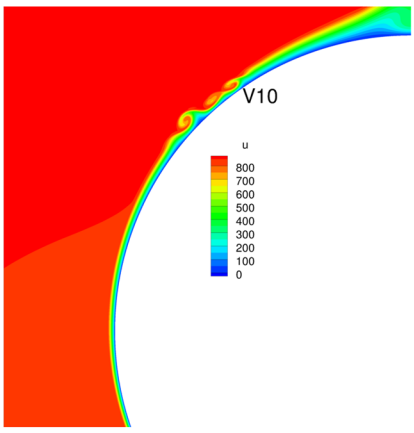

(d) Single wavelength forcing

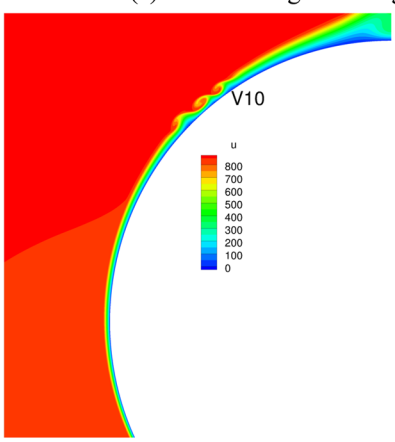

(e) Half wavelength forcing

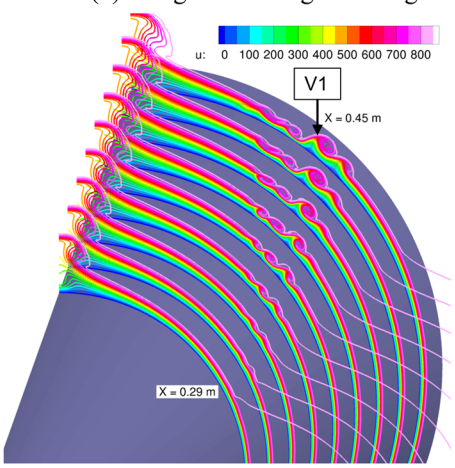

(f) Multiple axial stations for the case with single wavelength forcing (mirror image of vortex pattern from part (b)). Distance between each pair of adjacent stations is 0.02 m. V1 denotes the strongest vortex within the pattern.

Fig. 2 Axial velocity contours at $X = 0.4$ m for roughness distribution with varying azimuthal extent. Parts **a** through **e** indicate the half cone viewed from upstream, with the leeward ray at the top

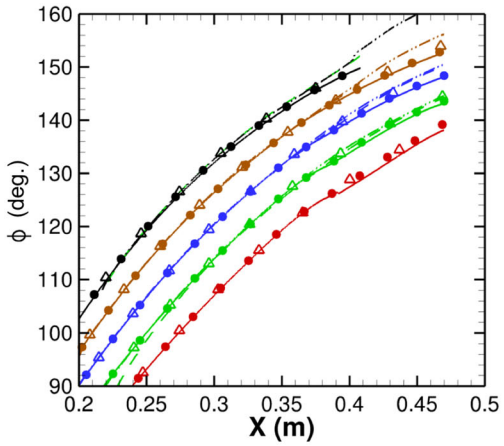

(a) Vortex trajectories. Colors distinguish between five different vortices from the vortex patterns.

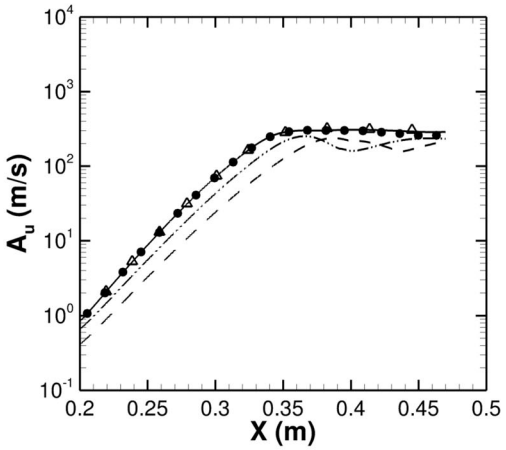

(b) Peak vortex amplitude (corresponding to vortex trajectory in blue from part (a) of the figure) as measured by maximum velocity perturbation associated with each forcing distribution.

Fig. 3 Comparison of vortex characteristics associated with different azimuthal distributions of roughness height. The line/symbol types indicate azimuthal extent of roughness distribution (solid: periodic, dashed: half wavelength, dash-dot: single wavelength, filled circles: three wavelengths, open triangles: five wavelengths)

variation in the azimuthal direction. However, it is easiest to distinguish between the separate vortex structures on the basis of their signature at the surface and the surface heat flux just happens to be a convenient, scalar quantity to bound the azimuthal range of each vortex structure. Other quantities such as wall shear perturbation could have been used as well, but wall shear is a vector quantity and, therefore, we deemed the heat flux to be a more convenient measure. Specifically, the vortex structures were deemed to be bounded by each pair of adjacent minima in the azimuthal distribution of the surface heat flux perturbation. The trajectories corresponding to the centerlines of selected stationary vortices from the various cases in Fig. 2 are shown in Fig. 3a. Specifically, the figure shows the four vortices detected within the compact vortex patterns of Figs. 2d, e, as well as an additional, (i.e., fifth) inboard vortex from the other three cases. The extra vortices seen in Figs. 2a–c are not included in this figure. The ordinate in Fig. 3a denotes the azimuthal angle φ with respect to the windward plane, which increases to 180 degrees at the leeward plane as indicated in the schematic from Fig. 1. Figure 3a shows that the vortex trajectories for all five roughness distributions align very well with each other, except for some small discrepancies in the downstream portions of the trajectories ($X > 0.35$ m) that are likely to be associated with nonlinear effects at higher vortex amplitudes. The overall comparison in Fig. 3a suggests that the vortex trajectories are insensitive to the azimuthal extent of the forcing, at least for the cases displayed in Figs. 2 and 3.

The amplitude A_u of each crossflow vortex plotted in Fig. 3a was determined as the peak value of the velocity perturbation parallel to the vortex trajectory at each axial location. The amplitude of the dominant crossflow vortex from each of the two compact roughness cases (Fig. 2d–e), along with the amplitude of the vortex along the same trajectory from the other three cases (which corresponds to vortex 8 from the periodic case of Li et al. [31]) is plotted as functions of the axial coordinate in Fig. 3b. Figure 3b shows that the amplitude evolution curves in all cases are nearly parallel to each other until the nonlinear effects come into play. The distances between the parallel evolution curves indicate the influence of the azimuthal distribution of roughness height on the effective initial amplitude of the dominant vortex.

The amplitude evolution curves from Fig. 3b demonstrate that the vortex amplitudes for the three-wavelength and five-wavelength forcing, respectively, are nearly the same as the vortex amplitude in the periodic-forcing case. The similarity in amplitude evolution implies that a nearly quasiperiodic behavior can be established for roughness extents that are as small as three azimuthal wavelengths. In this case, at least, further extensions of the roughness extent do not contribute significantly to the amplitude of the central vortex. As a result of the considerably larger initial amplitude for the noncompact roughness configurations, the vortex corresponding to blue trajectories in Fig. 3a) achieves nonlinear amplitude levels just upstream of $X = 0.35$ m and remains in a quasisaturated state within the downstream portion of the computational domain. The amplitude of the dominant vortex in the single-wavelength case reaches its peak value just downstream

of $X = 0.36\,\mathrm{m}$ and exhibits a weak oscillatory pattern thereafter. This oscillatory evolution of the vortex amplitude is associated with a cyclic energy exchange between the fundamental mode corresponding to the vortex wavelength and the mean flow distortion induced by nonlinear effects [83]. The vortex amplitude in the half-wavelength case displays a similar behavior, except that its evolution lags behind that in the other four cases. The post-saturation vortex amplitudes in the two limiting cases of a compact vortex pattern are similar to each other, but remain somewhat lower than the peak vortex amplitude achieved in the remaining three cases with larger extents of roughness height distribution.

4 High-frequency instabilities of a compact vortex pattern

In this section, the DNS data are used to assess the accuracy of secondary instability predictions for the compact vortex pattern excited by the single-wavelength, stationary forcing as shown earlier in Fig. 2f. This vortex pattern is relatively compact in comparison with the quasiperiodic vortex system studied by Li et al. [32], and hence, its instability characteristics must be analyzed in the context of the entire vortex pattern, unlike the previous analysis of the secondary instability of a single vortex from the quasiperiodic pattern in Ref. [32]. The secondary instability analysis for the compact pattern does not involve the ad hoc simplifications adopted during the prior analysis of a quasiperiodic vortex pattern, namely, the conversion of the azimuthally inhomogeneous basic state from Fig. 2a to a locally periodic flow and the assumption that the secondary disturbances amplify along a given stationary vortex rather than in some oblique direction with respect to the vortex axis. In this section, we will first analyze the local stability characteristics via planar eigenvalue analysis [75] and then use plane marching PSE [32,76] to predict the overall amplification of specific secondary instability modes. As noted in Ref. [32], the quasiparallel analysis does include the effects of transverse surface curvature associated with the conical surface; however, the effects of mean flow variations along the vortex trajectory are neglected in the local eigenvalue computations. The mode shapes based on the local computations are used to initiate the marching process for the plane marching PSE, which account for both surface curvature and the nonparallel effects on the downstream amplification of the secondary instability modes.

In general, the compact pattern of crossflow vortices is found to support two different types of unstable, high-frequency, secondary instability modes. One of them originates as Mack's second mode instabilities in the upstream region, where the amplitude of the stationary crossflow pattern is still small, and hence, the basic state closely resembles the unperturbed boundary layer over the cone at angle of attack. Mack's second mode instabilities have generally been studied in the context of 2D or axisymmetric boundary-layer flows that are invariant along the spanwise/azimuthal coordinate. In the context of those flows, the second mode instabilities correspond to acoustic disturbances that are trapped within the region of relative supersonic flow within the inner part of the boundary layer. The frequencies of these trapped acoustic modes are closely linked to the local thickness of the underlying boundary layer. Accordingly, at any fixed location, Mack's second mode waves in 2D/axisymmetric boundary layers are unstable over a relatively narrow range of frequencies or, conversely, a fixed frequency disturbance amplified over a narrow range of locations if the boundary-layer thickness continues to increase along the streamwise direction. In the present case, however, the basic state in the upstream part of the region of interest is close to the unperturbed boundary layer over the yawed cone, which decreases in thickness from the leeward to the windward plane of symmetry. Thus, the Mack mode instabilities in this region correspond to the generalization of the classic second-mode instabilities to an azimuthally inhomogeneous flow. Therefore, following the terminology from Li et al. [32], this family of modes is denoted with the prefix MM in this paper. As the crossflow vortices continue to gain in strength, the MM instabilities continue to get amplified and, often, at a higher rate, in contrast to Mack mode instabilities in the unperturbed boundary layer, which would have begun to decay beyond a moderate distance from the initial onset of instability. In other words, the MM modes behave as primary instabilities in the upstream region (where the crossflow disturbances are weak) and morph into secondary instabilities farther downstream when the crossflow vortices have become sufficiently strong.

There exist additional families of unstable modes, but they emerge only after the crossflow vortices have become sufficiently strong. Thus, at the onset of their amplification, the latter modes are equivalent to purely secondary instability modes associated with localized instabilities of the shear layer that bounds the crossflow vortex pattern, and hence, these modes are denoted with the suffix SI. As seen later, the MM modes also become concentrated in the shear layer region when the crossflow vortices become strong and may have similar mode shapes and amplification rates as the SI modes. In that regard, the classification of the instability modes as MM or SI modes pertains to the locations where those modes first become unstable. The MM modes have

a dual behavior, namely, primary Mack mode waves in the upstream limit and secondary instabilities in the downstream region. On the other hand, the SI modes owe their amplification to the localized shear layers induced by finite amplitude crossflow vortices. This is a crucial point that must be kept in mind in order to avoid any misinterpretation of the mode notation.

It is worth mentioning that lower-frequency traveling crossflow modes that are modulated by the stationary crossflow vortices were also found in the eigenvalue spectra within the downstream region, but their mode shape extended beyond the azimuthal boundaries of the selected domain for the stability analysis. Similar to Li et al. [32], the focus of this work is on the high-frequency instabilities that are concentrated within the compact vortex pattern, and hence, the lower-frequency modes are not further discussed within this paper.

For the compact crossflow vortex pattern of interest in this paper, the fluctuations associated with both MM and SI modes can extend over a majority of the azimuthal extent of the vortex pattern. However, the peak fluctuations associated with any given mode typically occur inside a single crossflow vortex from the overall pattern. The base flow contours from Fig. 2f indicate that there are two prominent crossflow vortices at $X = 0.33$ m (third station from the left), whereas an additional vortex becomes visible by $X = 0.37$ m. For simplicity, the dominant vortex on the windward side is denoted as V1 from here on, whereas the adjacent vortex on the leeward side of V1 (i.e., corresponding to the middle vortex at $X = 0.37$ m) will be denoted as V2 in the remaining paper. The remaining vortices do not play a significant role in the amplification of secondary instabilities.

Both MM and SI modes of secondary instability are subclassified according to whether the peak fluctuations are concentrated in the windward vortex (vortex V1) or in the adjacent vortex V2. Because the remaining vortices are relatively weak, the peak fluctuations associated with all dominant high-frequency instability modes occur within vortex V1 or vortex V2. Thus, mode MMV1 corresponds to the continuation of the Mack mode that induces peak fluctuations within the vortex V1. As described later, the modal peak may shift to a different vortex in the far downstream region, after the crossflow vortices have reached large amplitudes and begin to interact strongly with each other. However, the modal notation adopted herein is based on the location of peak fluctuations within the initial region of instability and that is also representative of a majority of the overall computational domain.

4.1 Local, quasiparallel secondary instability predictions for a compact vortex pattern

Growth rate predictions based on quasiparallel secondary instability analysis for the single-wavelength source corresponding to Fig. 2f are shown in Fig. 4. As mentioned previously, the traveling crossflow modes are beyond the scope of the present study and their eigenvalues were not converged for the selected azimuthal domain. Hence, those modes have been excluded from the eigenvalue spectra in Fig. 4. Representative mode shapes of $|u'|$ fluctuations associated with the peak growth rate frequency at two selected stations are shown in Fig. 5, where the flood contours of normalized disturbance amplitude are superposed with line contours associated with the axial base flow velocity across the cross-section of the compact vortex pattern. The base flow contours from Fig. 5 (as well as those seen earlier in Fig. 2f) indicate that there are two visible crossflow vortices at $X = 0.33$ m, whereas an additional crossflow vortex has gained sufficient amplitude by $X = 0.364$ m. As mentioned earlier, the vortex on the windward side within this range of locations is denoted as V1, whereas the vortex adjacent to V1 (i.e., the middle vortex at $X = 0.364$ m) is denoted as V2 herein. The third vortex (V3), which has just emerged on the leeward side of the vortex pattern near $X = 0.364$ m, is the weakest of the three vortices.

At the most upstream station shown in Fig. 4a, there are two unstable modes. The narrow frequency bandwidth of these modes along with the associated mode shapes (not shown here) reveals those modes to be Mack's second mode instabilities concentrated in the vicinity of crossflow vortices V1 and V2, respectively. The peak growth rate of the Mack mode that is colocated with V1 (and, hence, is denoted as Mack mode MMV1 in Fig. 4) is slightly larger than that associated with Mack mode MMV2 that is located along vortex V2. Similar to Mack's second mode instabilities, these modes are unstable over a relatively narrow range of frequencies and support significant fluctuations within the inner part of the boundary layer. Although not shown, at further upstream locations where the stationary crossflow disturbances are even weaker, the MMV1 and MMV2 modes reduce to the generalization of the classic second-mode instabilities to a fully 3D boundary layer with slow azimuthal variation. The peak growth rates of both MMV1 and MMV2 modes increase from $X = 0.313$ m to $X = 0.33$ m. In addition, the frequency range of the growth rate lobe connected with the MMV2 modes increases significantly across these two locations, with Fig. 4b for $X = 0.33$ m indicating a

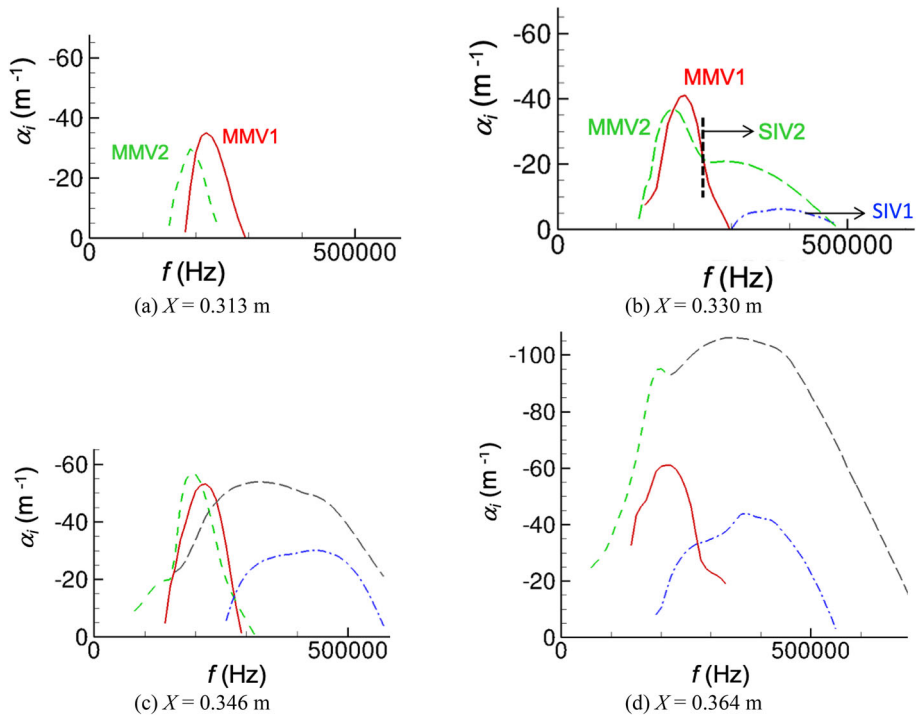

Fig. 4 Growth rate as function of frequency for dominant secondary instability modes at selected axial stations (red, solid: mode MMV1, green, dashed: (nominal) mode MMV2, blue, dash-dot: mode SIV1, black, dashed: mode SIV2)

frequency bandwidth that is nearly three times larger than that at $X = 0.313$ m. The growth rate lobe shown by the green curve clearly indicates two distinct subregions, namely, a narrow lobe at the low-frequency end that displays a clear maximum at approximately 200 kHz and closely resembles the classic growth rate behavior of Mack's second mode instabilities that was also seen at $X = 0.313$ m in Fig. 4a, and a second lobe at higher frequencies that displays a flatter peak in the growth rate spectrum. The latter behavior is attributed to the strengthening of the stationary crossflow vortex from $X = 0.313$ m to $X = 0.33$ m and, indeed, the mode shapes at the higher frequencies are primarily concentrated away from the surface, within the shear layer region that bounds the vortex structure V2. Thus, the higher-frequency part of the green curve in Fig. 4(b) is denoted as the SIV2 modes. An illustrative mode shape for these modes may be seen in Fig. 5c. An additional unstable mode corresponding to SI modes emerges at $X = 0.33$ m, as indicated by the blue curve in Fig. 4b. Farther downstream, at $X = 0.346$ m, the previously Mack mode MMV2 with a dual character at $X = 0.33$ m has split into two distinct modes, a Mack mode and a higher-frequency SI mode. As the crossflow vortices continue to become stronger from $X = 0.346$ m to $X = 0.364$ m, the peak growth rates of all four modes increase significantly, and particularly so for the modes riding on vortex V2. Furthermore, the frequency range of unstable disturbances now stretches from very low values to frequencies that are as high as approximately 600 kHz. However, subsequent results will show that, because the high-frequency modes come into play much later, those high-frequency disturbances do not correspond to large amplification ratios and that the peak N-factors within the domain of interest correspond to disturbance frequencies in the vicinity of 240 kHz.

Figure 5a, b shows that, in the presence of low- to modest amplitude crossflow vortices, the location of peak $|u|$' fluctuations associated with the MMV1 mode moves farther away from the wall and into the inclined shear layer bounding the crossflow vortex. Yet, the $|u|$' levels in the lower part of the boundary layer remain weak but significant. On the other hand, the SI modes tend to be highly concentrated in the localized shear layers away from the surface (Fig. 5c), but our computations (not included here) have shown that, at certain location, weak but significant fluctuations may be observed underneath the off-body location of the peak fluctuation. Again, we emphasize that the primary distinction between the two modes is related to their upstream origin. However, in so far as the MM modes have a significant surface signature over a longer distance, those fluctuations would be more easily measured via surface-based instrumentation. Overall, the secondary instability results from

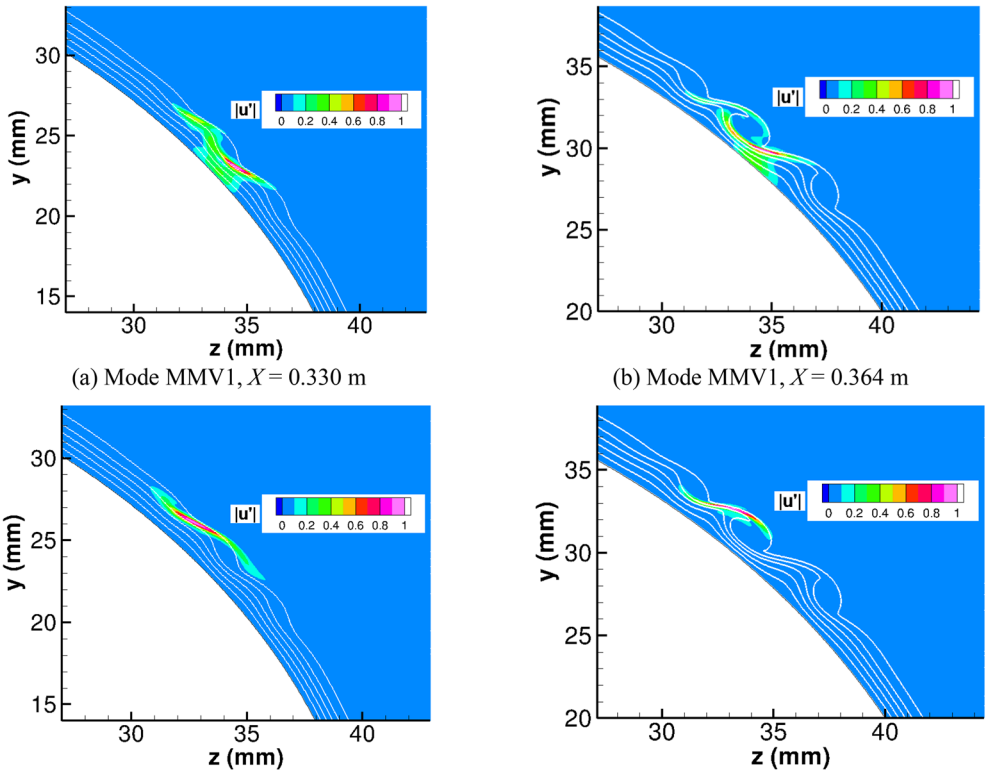

(a) Mode MMV1, $X = 0.330$ m

(b) Mode MMV1, $X = 0.364$ m

(c) Mode SIV2, $X = 0.330$ m

(d) Mode SIV2, $X = 0.364$ m

Fig. 5 $|u|'$ eigenfunctions corresponding to most unstable frequencies from Fig. 4b and d, respectively, for both Mack modes and SI modes. The azimuthal angle φ increases from right to left

Figs. 4 and 5 indicate that the frequencies and mode shapes associated with the compact vortex pattern are rather analogous to those found earlier for a quasiperiodic vortex pattern [32].

4.2 Nonparallel evolution of secondary instability modes

Next, we consider the nonparallel evolution of secondary instability modes as predicted by the plane marching PSE. The PSE marching begins near the lower branch neutral station identified from the local eigenvalue analysis, and the eigenfunctions from that analysis are used as the inflow condition for the marching process. Mode shapes of $|u'|$ fluctuations associated with two representative instability modes of types MM and SI are shown in Fig. 6a, b, respectively. Both figures display the crossplane contours of the meridional component $|u'|$ at $f = 240$ kHz, superposed with gray shade contours of the logarithmic amplification factor (i.e., N-factor) based on the surface pressure fluctuations in each case. Subsequent results will show that $f = 240$ kHz falls within the range of most amplified secondary instabilities within the vortex pattern of interest here. Figure 6a shows that, as the amplitude of the crossflow vortices increases from relatively small values near the upstream end of the computational domain to larger, yet modest amplitudes near $X = 0.330$ m, the location of peak $|u'|$ fluctuations associated with the MMV1 mode moves away from the wall and into the inclined shear layer bounding the stationary crossflow vortex. The $|u'|$ levels in the lower part of the boundary layer are weaker but not negligible. Although not shown, a similar behavior is noted for the MMV2 mode shapes, except that the peak fluctuations are located within the vortex V2. On the other hand, the SI modes are primarily concentrated in the localized shear layers away from the surface as indicated by the SIV2 mode shape in Fig. 4b. Similar findings were reported by Li et al. [31] for a quasiperiodic vortex pattern due to an azimuthally periodic source, but they also found certain cases where weak but significant SI mode fluctuations occurred below the peak inside the shear layer.

The axial evolution of the logarithmic amplification ratio, i.e., the N-factor, associated with fixed-frequency secondary disturbances of the MMV1 and MMV2 type is shown in Figs. 7a, b, respectively. Because the N-

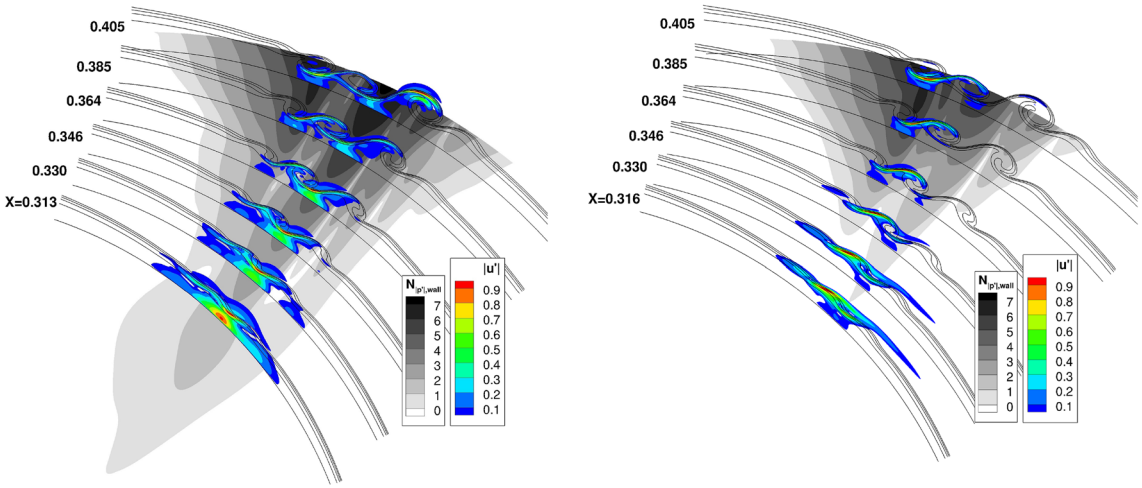

(a) Mode MMV1 (b) Mode SIV2

Fig. 6 Contours of disturbance amplitudes ("mode shapes") based on $|u'|$ fluctuations at f = 240 kHz and selected axial stations. At each station, the peak fluctuation amplitude is normalized to unity. To highlight the regions of strong fluctuations at multiple axial stations, contours are shown only within the boundary-layer region. Gray-shaded contours along the cone surface indicate N-factor distribution based on the surface pressure fluctuations

factors for the SI modes are uniformly lower than those of the MM modes, only the results for the SIV2 mode are shown in Fig. 7c for the purpose of illustration. N-factors for the SIV1 mode are even lower than those of mode SIV2, i.e., maximum N-factor of 6 at the end of the domain, and hence, they are omitted from Fig. 7. The MM modes typically display an initial region of growth that is dominated by the Mack mode instability, followed by a downstream region of accelerated growth (manifested via the increased slope of N-factor curves) as the Mack modes get further destabilized by the finite amplitude crossflow vortices. The envelope of the N-factor curves in Fig. 7a is reflective of the Mack mode behavior up to approximately $X = 0.30$ m, whereas the onset of shear layer instability is delayed until $X = 0.32$ m for the MMV2 modes, perhaps because the vortex V2 lags behind the vortex V1 in terms of its amplitude saturation. The SI modes owe their amplification entirely to the large amplitudes of the crossflow vortices, and hence, their amplification curves do not include the initial region of growth encountered by the MM modes when the crossflow vortices are relatively weak. In the downstream region, where both MM and SI modes coexist, the mode shape and growth rate characteristics of both modes are similar to each other. However, because of the initial phase of growth as predominantly Mack modes of a quasihomogeneous boundary layer, the N-factors for the MM modes are generally higher than those of the SI modes, at least for the range of locations considered in this paper. Thus, it is the prior history of the MM modes that sets them apart from the SI modes, and it would also enable those modes to play a potentially more important role than the SI modes during the transition process.

4.3 Disturbance evolution based on DNS and comparison with plane marching PSE

To assess the accuracy of the secondary instability analysis presented above, DNS is used to investigate the propagation of high- frequency instabilities in the presence of the azimuthally localized vortex pattern due to single-wavelength forcing as shown earlier in Fig. 2f. Disturbances at various selected frequencies were introduced via azimuthally uniform, time harmonic, surface suction and blowing over an axially localized strip near $X = 0.28$ m. The suction/blowing distribution is azimuthally uniform and harmonic in time, consisting of multiple frequencies ranging from $f = 20$ kHz to $f = 480$ kHz as mentioned previously. The grid spacing of the DNS grid is based on prior experience while applying the code to similar problems involving transitional and fully turbulent flows. The overall size of the grid corresponds to $2000 \times 450 \times 450$ points in the axial, azimuthal, and radial directions, respectively. The azimuthal grid is clustered within the region of the compact vortex pattern. The axial grid spacing is reduced near the region of forcing, in order to resolve the receptivity process. Magnitudes of surface pressure fluctuations (normalized by a suitably chosen constant) at selected disturbance frequencies, based on a discrete Fourier transform of the computed data, are plotted in Fig. 8a–f.

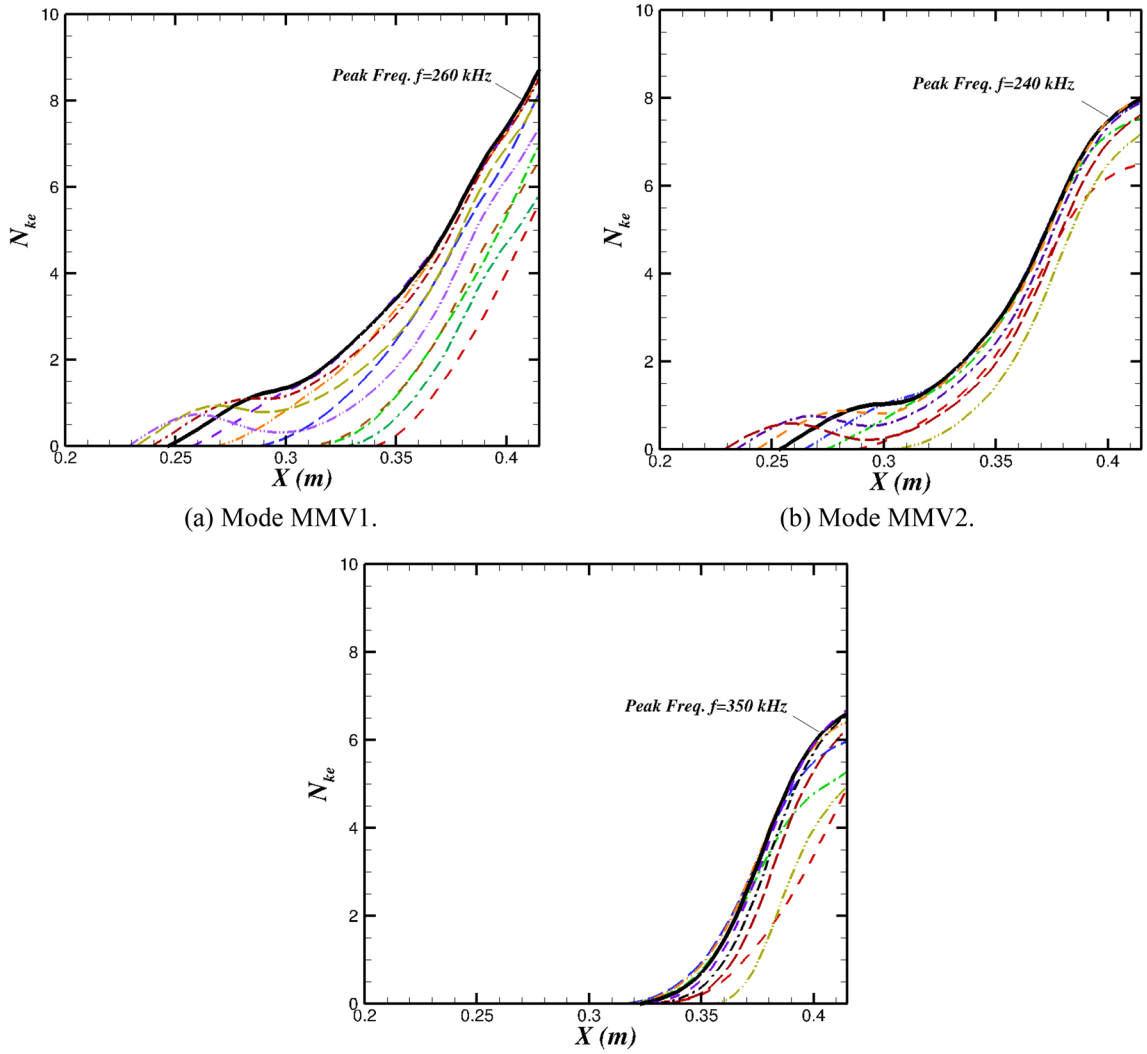

(a) Mode MMV1.

(b) Mode MMV2.

(c) Mode SIV2.

Fig. 7 Amplification characteristics of dominant secondary instability modes of the compact crossflow vortex pattern. Each curve in these figures denotes the N-factor evolution of a fixed frequency disturbance from a specified family of modes

Because of the strong destabilizing influence of stationary crossflow vortices, the azimuthal regions of the highest amplitudes of secondary disturbances up to $f = 320$ kHz correspond to the region of the crossflow vortices (Fig. 8a–d). Figure 8a also shows a second peak with weaker fluctuations near the $\varphi = 160$ deg azimuthal location. There are no significant crossflow vortices in this region and the latter peak is associated with purely Mack mode instabilities of the underlying boundary layer over the cone. As the disturbance frequency increases from Fig. 8a–f, the azimuthal region of Mack mode fluctuations shifts progressively toward the windward meridian. The windward shift at increasing frequencies is consistent with the fact that the frequency of Mack's second mode instabilities is approximately tuned to the local thickness of the boundary layer, which increases from the windward ray toward the leeward ray. In the region of approximately $0.35\,\text{m} < X < 0.40\,\text{m}$, Mack mode fluctuations at the relatively low frequency of $f = 120$ kHz are unstable only within the region of the relatively thicker boundary layer near φ 160 deg (Fig. 8a). At the significantly higher frequency of $f = 320$ kHz (Fig. 8d), the region of Mack mode fluctuations has moved to significantly lower azimuthal angles and now appears on the windward side of the crossflow vortex pattern. Because there are no crossflow disturbances in this region, the underlying basic state is the same as the quasi-homogenous boundary layer; these fluctuations essentially represent primary instabilities in the form of Mack's second mode waves in the

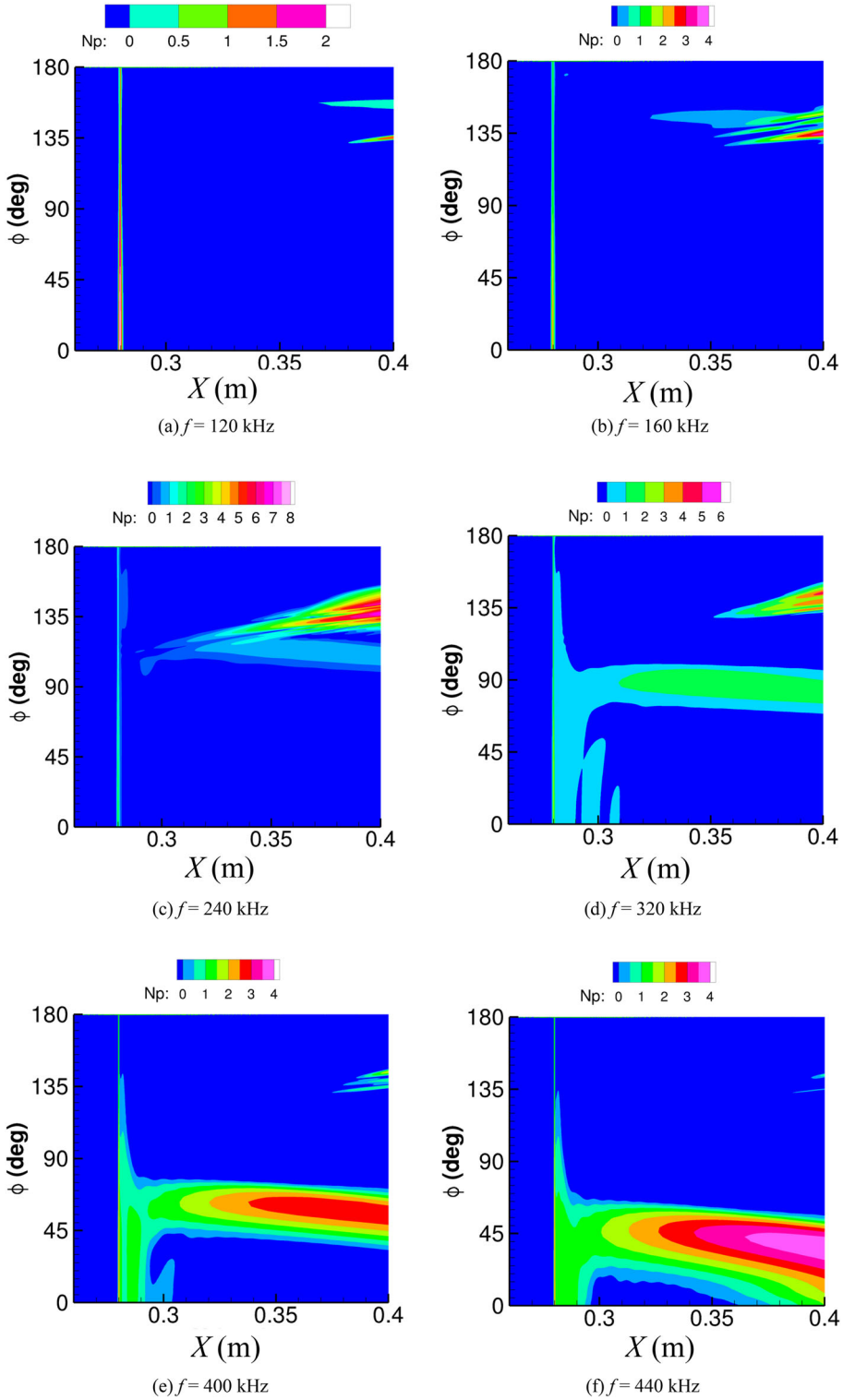

(a) $f = 120$ kHz (b) $f = 160$ kHz

(c) $f = 240$ kHz (d) $f = 320$ kHz

(e) $f = 400$ kHz (f) $f = 440$ kHz

Fig. 8 $|p|'$ contours on cone surface for selected forcing frequencies (continued on next page)

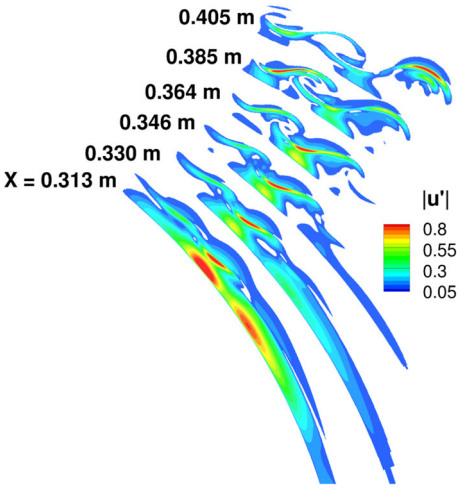

Fig. 9 Contours of unsteady fluctuation in axial velocity component u (i.e., "mode shapes") at f = 240 kHz for selected axial stations. At each station, the peak fluctuation amplitude is normalized to unity. To highlight the regions of strong fluctuations at multiple axial stations, contours are shown only within the boundary-layer region. Azimuthal range of locations corresponds to the region of the compact vortex pattern as indicated by the presence of progressively stronger rollup at the downstream locations

unperturbed boundary layer over the cone. These results represent a byproduct of the DNS and provide useful extra insights into the growth of Mack's second mode instabilities over a cone at angle of attack.

At $f = 440$ kHz (Fig. 8f), even the boundary-layer flow along the windward ray is seen to exhibit a modest growth of Mack mode fluctuations. As mentioned previously, the frequency of Mack's second mode instabilities is closely related to the thickness of the boundary layer, which explains the windward shift in the region of peak fluctuations as the frequency is increased. Figure 8 also shows that the amplification of the Mack mode fluctuations becomes progressively stronger as the disturbance frequency increases from 320 to 440 kHz. However, the highest overall amplification factors over the entire cone surface correspond to a disturbance frequency of 240 kHz, which is in approximate agreement with the N-factor predictions based on secondary instability theory. Overall, the results in Fig. 8 indicate a qualitative similarity to the growth rate spectra in Fig. 4 based on the secondary instability theory.

Another interesting aspect of the disturbance contours presented in Fig. 8 involves the opposite orientations of the loci of peak fluctuation amplitudes corresponding, respectively, to the secondary instabilities of the crossflow vortex pattern and the Mack's second mode instabilities within the unperturbed, 3D mean boundary layer on either side of that vortex pattern. The orientation of the stationary crossflow vortices tends to be within a few degrees of the direction of the inviscid streamlines, which move gradually toward the leeward ray along the downstream direction. Because the secondary instabilities derive their energy from the disturbance energy production associated with the high shear regions created by the crossflow vortices, the locus of highest secondary instability amplitudes is closely aligned with the trajectory of the crossflow vortex pattern. The leeward inclination of this locus is clearly seen at $f = 240$ kHz (Fig. 8c). On the other hand, the locus of peak fluctuations associated with the Mack's second mode instabilities in the unperturbed boundary layer is clearly tilted toward the windward ray as seen most clearly at $f = 440$ kHz in Fig. 8f.

Mode shapes of $|u|$' perturbations at selected locations from the DNS flowfield are shown in Fig. 9. The peak fluctuation level at each station has been normalized to unity. The mode shape at $X = 0.313$ m indicates two separate azimuthal regions of high fluctuations. The windward peak corresponds to Mack mode fluctuations inboard of the crossflow vortex pattern, whereas the other peak corresponds to the secondary instability modes of the crossflow vortex pattern as seen in Fig. 5. The computed $|u'|$mode shapes at $X = 0.330$ m and $X = 0.364$ m within the region of vortex V1 are quite similar to the Mack mode eigenfunctions predicted by the quasiparallel secondary instability theory (Fig. 5a, b, respectively).

The PSE mode shapes for the $|u|$' fluctuations due to mode MMV1 (Fig. 6a) are also similar to the DNS results from Fig. 9. Indeed, the PSE predictions are also successful in capturing a rather subtle feature of the mode shapes from the DNS results. Specifically, we note that the MMV1 mode shapes in Fig. 6a indicate a switchover in the location of peak $|u|$' fluctuations from the shear layer of vortex V1 at $X = 0.364$ m to the shear layer of vortex V2 at $X = 0.385$ m and then back to the vortex V1 at $X = 0.405$ m. An identical behavior

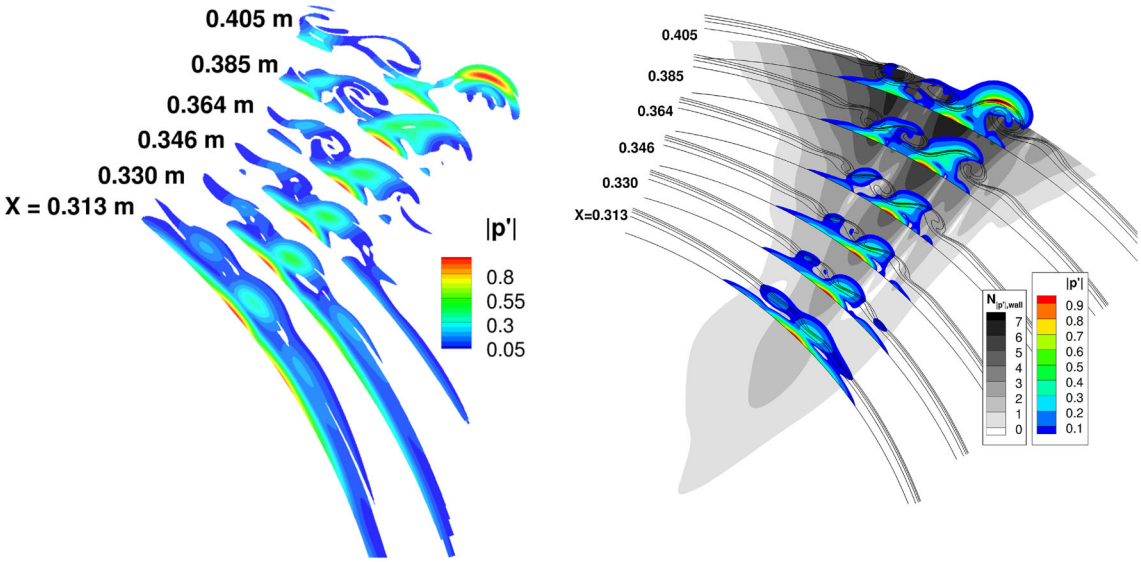

(a) DNS. (b) Plane marching PSE (mode MMV1).

Fig. 10 Contours of normalized disturbance amplitudes ("mode shapes") based on pressure fluctuations at f = 240 kHz and selected axial stations. At each station, the peak fluctuation amplitude is scaled to unity. To highlight the regions of strong fluctuations at multiple axial stations, contours are shown only within the boundary-layer region

is also observed in the DNS calculations, suggesting that the mode MMV1 may account for a dominant portion of the disturbance field from the DNS solution.

Mode shapes of $|p|$' perturbations at selected locations from the DNS flowfield and the corresponding PSE predictions for mode MMV1 at the same locations are shown in Fig. 10a, b, respectively. The DNS mode shape at $X = 0.313$ m indicates two separate azimuthal regions of high-amplitude fluctuations. The windward peak corresponds to Mack's second mode fluctuations inboard of the crossflow vortex pattern, whereas the other peak corresponds to the secondary instability modes of the crossflow vortex pattern as seen from the surface pressure fluctuations in Fig. 8c. The inboard fluctuations are excited as Mack's second mode (primary) instabilities of the unperturbed boundary-layer flow without any crossflow vortices. The wall forcing in DNS extends across the entire circumference of the cone and, hence, can excite the instability modes of the boundary-layer regions both with and without the crossflow vortices. However, the instabilities modes of the boundary-layer flow outside of the crossflow vortex packet were neither targeted nor expected to be captured within the PSE predictions. Between $X = 0.330$ m and $X = 0.385$ m, the peak pressure fluctuations in DNS are located close to the surface underneath vortex V1, similar to the PSE predictions for mode MMV1 in Fig. 6b. As a result of the continued interaction with the underlying crossflow vortex, the peak pressure fluctuations at $X = 0.405$ m have shifted away from the surface and to the top of the crossflow vortex structure. The same trend is also captured by the MMV1 mode predictions based on PSE. The DNS solution also indicates relatively stronger $|p|$' fluctuations within vortex V2 for $X \geq 0.385$ m, and that feature is again predicted by the PSE.

Frequency spectra of the disturbance N-factor from the DNS calculations and those of mode MMV1 from the PSE computations are shown in Fig. 11a, b, respectively. Both N-factors are based on the integral of the disturbance kinetic energy across the cross-section of the vortex pattern. The PSE N-factors are defined with respect to the neutral location. Because of the proximity of the neutral station to the wall-forcing location, the neutral station cannot be easily defined from the DNS calculation, and therefore, the DNS N-factors are shifted vertically so that the N-factor for $f = 240$ kHz matches the PSE prediction at $X = 0.313$ m. We observe that the peak of the N-factor spectra corresponds to nearly the same frequency in both the DNS and the PSE results. The peak frequency from the DNS corresponds to $f = 240$ kHz, subject to some uncertainty due to the relatively coarse frequency resolution of the DNS analysis ($\Delta f \approx 40$ kHz). The peak frequency from the PSE calculations is slightly higher, between $f = 240$ kHz and $f = 260$ kHz, depending on the axial location; however, the discrepancy in peak frequency could, in part, be caused by the finer resolution of the PSE calculations ($\Delta f \approx 20$ kHz).

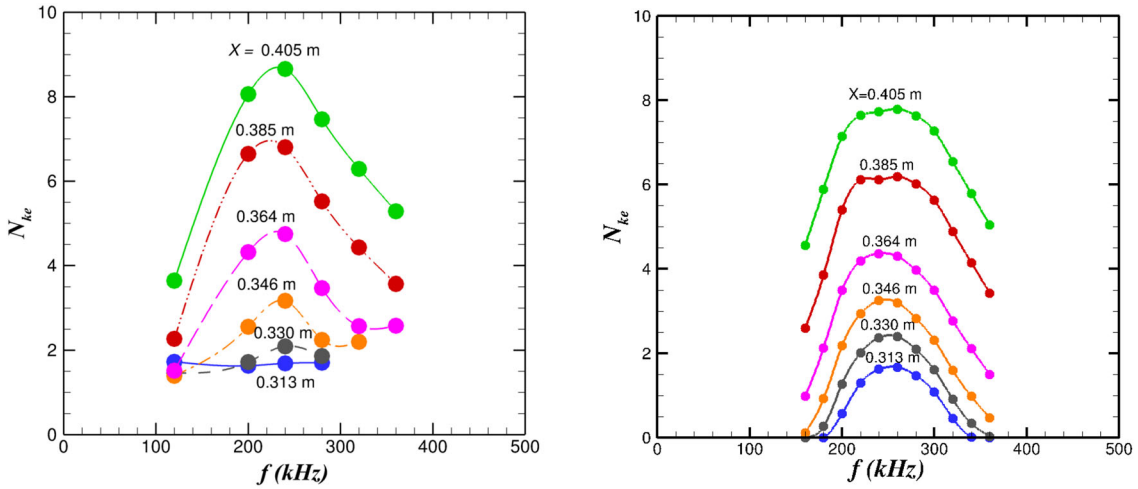

(a) DNS. (b) Plane marching PSE (mode MMV1).

Fig. 11 N-factor spectra based on disturbance kinetic energy at selected axial stations. To focus on the effects of the compact crossflow pattern, fluctuations at azimuthal locations beyond the crossflow pattern are ignored in this analysis.

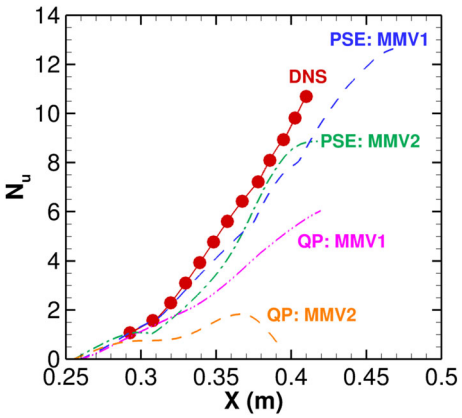

Fig. 12 N-factor evolution for f =240 kHz

Figure 12 shows the N-factor evolution for high-frequency instabilities with $f = 240$ kHz as computed via the DNS, plane marching PSE, and the quasiparallel predictions. Over a significant range of distances, the PSE-based N-factor curves for modes MMV1 and MMV2 are rather close to each other. To begin with, the N-factor for the MMV2 mode is slightly less than that of the MMV1 mode. However, near $X \approx 0.36$, the MMV2 N-factor crosses above the N-factor curve for the MMV1 mode. A notable difference between the evolution of these two modes involves their far downstream behavior near $X = 0.4$, where the MMV2 mode ceases to amplify, whereas the MMV1 mode continues to grow across the entire region included in the basic state calculation for the crossflow vortex pattern. The domain for the DNS continues up to $X = 0.41$, and the continued rise of the N-factor in the DNS solution is analogous to the MMV1 mode from the PSE predictions. This behavior is consistent with the mode shape similarity between the DNS solution and the MMV1 mode, and tends to confirm that the DNS solution is dominated by the MMV1 mode.

Figure 12 also shows that the N-factors based on the PSE predictions are in relatively good agreement with those inferred from the DNS solution, whereas the N-factors based on the quasiparallel predictions are substantially below the corresponding values from the PSE and DNS calculations. The difference between PSE and quasiparallel N-factors for the MMV1 mode near $X = 0.41$ is approximately $\Delta N \approx 3.5$, whereas the quasiparallel N-factor for the MMV2 is way below the N-factor values from both the PSE and DNS predictions; it reaches a peak value of less than 2 near $X = 0.37$ and decays rapidly beyond that location.

5 Summary and concluding remarks

The crossflow vortex patterns over a yawed cone are not exactly periodic in the azimuthal direction, even when the disturbance source is periodic. In general, an azimuthally nonuniform vortex pattern can arise either because of the azimuthal inhomogeneity of the unperturbed boundary layer at a nonzero angle of yaw as well as of the roughness height distribution over the cone surface. This paper described computations of stationary crossflow instability confined to a finite azimuthal width, with the goal of bridging the gap between the two limiting cases of azimuthally periodic and azimuthally compact crossflow vortex patterns. Simulation results indicate that the azimuthal distribution of forcing has a strong influence on the stationary crossflow amplitudes; however, the vortex trajectories are nearly the same for both periodic and localized roughness height distributions.

The high-frequency secondary instabilities of a compact vortex pattern were examined to help address the effects of azimuthal inhomogeneity across the pattern. Equally significant, this analysis addressed certain shortcomings of the previous analyses pertaining to the secondary instability of quasiperiodic vortex patterns. The linear secondary instability analysis for a compact crossflow pattern included both quasiparallel and nonparallel predictions and a quantitative comparison with the DNS results. Results have shown that the quasi-parallel predictions can reveal the general topology of instability modes and, to some extent, their approximate spatio-temporal characteristics. However, they do not provide accurate predictions of instability growth in the present case and lead to severe underprediction of the N-factors for the dominant instability modes. In contrast, the nonparallel plane marching PSE framework is able to yield predictions that agree more closely with the DNS results and the agreement between the two extends across mode shapes, dominant frequencies, as well as the N-factors of the most amplified instability modes. The PSE results also capture relatively subtle features of the DNS solutions in terms of a switchover in peak disturbance location from one vortex to another, and back shortly thereafter.

Secondary instabilities of azimuthally compact crossflow vortex patterns are qualitatively similar in terms of mode types, frequencies, and mode shapes to the secondary instabilities of azimuthally noncompact, quasiperiodic vortex patterns. However, whereas the previous analyses based on azimuthally periodic BCs imply that the secondary instability field extends over multiple crossflow vortices, the current analysis shows that even when the vortex pattern includes three dominant vortices, the prominent modes of secondary instability are confined to a single vortex in general. The present analysis also does not involve any ad hoc simplifications associated with making the azimuthally inhomogeneous basic state locally periodic in the azimuthal direction and the assumption that the secondary disturbances amplify along a given stationary vortex. If anything, the secondary instability presented herein appears to provide some justification to the latter assumption.

The frequencies of the most amplified secondary disturbances are in the range of 200 kHz to 360 kHz. This frequency range is approximately consistent with the frequencies measured in the experiments at Purdue University [22–24] and the Technical University of Braunschweig [21]. The present computations have also shown that the high-frequency secondary disturbances can achieve sufficiently large amplification factors to induce the onset of transition over the cone. The stationary crossflow disturbances are rather weak in the upstream part of the computational domain and the instability amplification in this region is dominated by instability modes that represent the generalization of the classic, Mack's second mode instabilities in 2D/axisymmetric boundary layers to the case of azimuthally inhomogeneous 3D boundary layers. These MM modes coexist with the so- called SI instabilities in the downstream region where the stationary crossflow vortices have become strong enough to sustain secondary instabilities. Computations reveal that the two mode types can have similar amplification rates and mode shapes in this region. The MM modes are differentiated from the SI modes primarily on the basis of their upstream origin (MM modes are present even when the vortex amplitude is small and SI modes emerge only after the stationary vortex has attained a large enough amplitude), but the two mode types may also exhibit some differences in terms of the relative strength of their fluctuations in the vicinity of the wall (MM modes having a stronger near-wall presence than the SI modes over a larger portion of their streamwise evolution). By virtue of the extra initial amplification of the modes originating from the Mack's second mode instability, the MM modes achieve higher amplification factors in this case and, therefore, are likely to play a more important role in the flow dynamics and the laminar-turbulent transition process. However, depending on the difference between the N-factors of the MM and SI modes, respectively, and their receptivity characteristics in the relevant disturbance environment, the SI modes could certainly produce a small to modest correction to the overall disturbance amplitudes.

Acknowledgements This work was performed as part of the Revolutionary Computational Aerosciences discipline under the Transformational Tools and Technologies project of the NASA Transformative Aeronautics Concepts Program. Computational

resources for this work were provided by the NASA High-End Computing (HEC) Program through the NASA Advanced Supercomputing (NAS) Division at Ames Research Center. MC would like to thank Prof. Steven Schneider and Dr. Joshua Edelman from Purdue University for several technical discussions. The authors also acknowledge Prof. Pino Martin from the University of Maryland for providing the original version of the DNS code used in this effort.

Declarations

Data availability statement The data and code used in this work are currently proprietary and confidential; it will be considered for public release in the future.

References

1. Mack, L.M.: Boundary-layer linear stability theory, in special course on stability and transition of laminar flow, AGARD Report No. 709, pp. 3.1–3.81 (1984)
2. Li, F., Choudhari, M.M., Chang, C.-L., Wu, M., Greene, P.T.: Development and breakdown of Görtler vortices in high speed boundary layers, AIAA Paper 2010–705 (2010)
3. Saric, W.S., Reed, H.L., White, E.B.: Stability and transition of three-dimensional boundary layers. Ann. Rev. Fluid Mech. **35**, 413–440 (2003)
4. Malik, M.R., Li, F., Choudhari, M., Chang, C.-L.: Secondary instability of crossflow vortices and swept-wing boundary-layer transition. J. Fluid Mech. **399**, 85–115 (1999)
5. Dougherty, N.S., Fisher, D.F.: Boundary layer transition on a 10-degree cone: wind tunnel/flight data correlation, AIAA Paper 80-0154 (1980)
6. King, R.A.: Three-dimensional boundary-layer transition on a cone at Mach 3.5, experiments in fluids, Vol. 13, No. 5, pp. 305–314 (1992)
7. Malik, M.R., Balakumar, P.: Instability and transition in three-dimensional supersonic boundary layers, AIAA Paper 1992-5049 (1992)
8. Hanifi, A., Dahlkild, A.A.: Some stability characteristics of the boundary layer on a yawed cone, AIAA Paper 1993-3048 (1993)
9. Sugiura, H., Tokugawa, N., Nishizawa, A., Ueda, Y., Ishikawa, H., Yoshida, K: boundary-layer transition on axisymmetric bodies with angles of attack in supersonic flow. In: Proceedings of 2003 Annual Meeting, Japan Society of Fluid Mechanics, (in Japanese), pp. 352–353 (2003)
10. Balakumar, P.: Stability of supersonic boundary layers on a cone at an angle of attack, AIAA Paper 2009-3555, 2009
11. Tokugawa, N., Choudhari, M., Ishikawa, H., Ueda, Y., Fujii, K., Atobe, T., Li, F., Chang, C.-L., White, J.: Transition along leeward ray of axisymmetric bodies at incidence in supersonic flow. AIAA J. **53**(12), 3737–3751 (2015). https://doi.org/10.2514/1.J054070
12. Choudhari, M., Tokugawa, N., Li, F., Chang, C.-L., White, J., Ishikawa, H., Ueda, Y., Atobe, T., Fujii, K.: Computational investigation of supersonic boundary layer transition over canonical fuselage nose configurations. In: Proc. of 7^{th} Intl. Conference on Computational Fluid Dynamics, Island of Hawaii, June 2012. http://www.iccfd.org/iccfd7/assets/pdf/papers/ICCFD7-2306_paper.pdf
13. Schuele, C.Y., Corke, T.C., Matlis, E.: Control of stationary crossflow modes in a Mach boundary layer using patterned passive and active roughness. J. Fluid Mech. **718**, 5–38 (2013)
14. Stetson, K.F., Thompson, E.R., Donaldson, J.C., Siler, L.G.: Laminar boundary layer stability experiments on a cone at Mach 8 – Part 3: sharp cone at angle of attack, AIAA Paper 85-0492 (1985)
15. Schneider, S.P.: Hypersonic Laminar-turbulent transition on circular cones and scramjet forebodies. Prog. Aerospace Sci. **40**, 1–5 (2004)
16. Swanson, E.: Boundary-layer transition on cones at angle of attack in a Mach 6 Quiet Tunnel, Ph.D. Dissertation, School of Aeronautics and Astronautics, Purdue University (2008)
17. Swanson, E., Schneider, S.P.: Boundary-layer transition on cones at angle of attack in a Mach-6 Quiet Tunnel, AIAA Paper 2010-1062 (2010)
18. Li, F., Choudhari, M., Chang, C.-L., White, J.: Analysis of instabilities in non-axisymmetric hypersonic boundary layers over cones, AIAA Paper 2010-4643 (2010)
19. Balakumar, P., Owens, L.: Stability of hypersonic boundary layers on a cone at angle of attack, AIAA Paper 2010-4718 (2010)
20. Li, F., Choudhari M., Chang, C.-L., White, J. A., Kimmel, R., Adamczac, D., Borg, M., Stanfeld, S., Smith, M.: Stability analysis for HIFiRE experiments, AIAA Paper 2012-2961 (2012)
21. Munoz, F., Heitmann, D., Radespiel, R.: Instability modes in boundary layers of an inclined cone at Mach 6. J. Spacecr. Rockets **51**(2), 442–454 (2014)
22. Ward, C.A.C., Henderson, R.O., Schneider, S.P.: Possible secondary instability of stationary crossflow vortices on an inclined cone at Mach 6, AIAA Paper 2015-2773 (2015)
23. McKiernan, G.R., Chynoweth, G.R., Edelman, J.B., McKenzie, J.A., Sweeney, C.J.: Instability and transition experiments in the boeing/AFOSR Mach 6 Quiet Tunnel, AIAA Paper 2015-2317 (2015)
24. Edelman, J., Schneider, S.P.: New measurements of the secondary instability of stationary crossflow waves in the Mmach-6 Quiet Tunnel, NATO-STO AVT-240 & RTG-082 Meeting on Hypersonic Boundary Layer Transition, Prague, Czech Republic, Oct. 15–16 (2015)
25. Craig, S.A., Saric, W.: Crossflow instability on a yawed cone at Mach 6, In: Medeiros, M.A.F., Meneghini, J.R. (Eds.) 8th IUTAM Symposium on Laminar-Turbulent Transition, Procedia IUTAM, Vol. 14, pp. 15–25 (2015)

26. Craig, S.A., Saric, W.S.: Experimental study of crossflow instability on a Mach 6 Yawed Cone, AIAA Paper 2015-2774 (2015)
27. Oliviero, N.B., Kocian, T.S., Moyes, A.J., Reed, H.L.: EPIC: NPSE analysis of hypersonic crossflow instability on yawed straight circular cone, AIAA Paper 2015-2772 (2015)
28. Stanfield, S., Kimmel, R.A., Adamczac, D., Juliano, T.: Boundary-layer transition experiment during reentry of HIFiRE-1. J. Spacecr. Rockets **52**, 637–649 (2015)
29. Juliano, T., Kimmel, R.A., Willems, S., Guelhan, A., Wagnild, R.: HIFiRE-1 boundary-layer transition: ground test results and stability analysis, AIAA Paper 2015-1736 (2015)
30. Li, F., Choudhari, M., Paredes, P.: Nonlinear evolution and secondary instability of crossflow disturbances in hypersonic boundary layer over a cone, NATO-STO AVT-240 & RTG-082 Meeting on Hypersonic Boundary Layer Transition, Prague, Czech Republic, Oct. 15-16 (2015)
31. Li, F., Choudhari, M., Paredes, P., Duan, L.: Secondary instability of stationary crossflow vortices in mach 6 boundary layer over a circular cone, NASA/TM-2015-218997 (2015)
32. Li, F., Choudhari, M., Paredes, P., Duan, L.: High-frequency instabilities of stationary crossflow vortices in a hypersonic boundary layer. Phys. Rev. Fluids **1**, 053603 (2016)
33. Moyes, A.J., Paredes, P., Kocian T.S., Reed, H.: Secondary instability analysis of crossflow on a hypersonic yawed straight circular cylinder, AIAA Paper 2016-0848 (2016)
34. Edelman, J., Schneider, S.P.: Secondary instabilities of hypersonic stationary crossflow waves. AIAA J. **56**(1), 182–192 (2018)
35. Niu, H., Yi, S., Liu, X., Juo, J., Jin, L.: Experimental investigation of Nosetip Bluntness effects on the hypersonic crossflow instability over a cone. Int. J. Heat Fluid Flow **86**, 108746 (2018)
36. Yates, H.B., Matlis, E., Juliano, T.J., Tufts, M.W.: Plasma-actuated flow control of hypersonic crossflow-induced boundary-layer transition. AIAA J. **58**, 2093–2108 (2020)
37. Corke, T.C., Arndt, A., Matlis, E.H., Semper, M.: Control of stationary crossflow modes in a Mach 6 boundary layer using patterned roughness. J. Fluid Mech. **856**, 822–849 (2018)
38. Kimmel, R.: Laminar-turbulent transition in a Mach 8 elliptic cone flow. AIAA J. **37**(9), 1080–1087 (1999)
39. Poggie, J., Kimmel, R.: Traveling instability waves in a Mach 8 flow over an elliptic cone. AIAA J. **38**(2), 251–258 (2000)
40. Kimmel, R.L., Poggie, J.: Transition on an elliptic cone at Mach 8, American Society of Mechanical Engineers ASME FEDSM97-3111 (1997)
41. Kimmel, R.L., Poggie, J., Schwoerke, S.N.: Laminar-turbulent transition in a Mach 8 elliptic cone flow. AIAA J. **37**(9), 1080–1087 (1999)
42. Holden, M.: Experimental studies of laminar, transitional, and turbulent hypersonic flows over elliptic cones at angle of attack. Air Force Office of Scientific Research Technical Report AFRL-SR-BL-TR-98-0142. Bolling Air Force Base, DC (1998)
43. Schmisseur, J.D., Schneider, S.P., Collicott, S.H.: Response of the Mach 4 boundary layer on an elliptic cone to laser-generated freestream perturbations, AIAA Paper 1999-0410 (1999)
44. Choudhari, M., Chang, C.-L., Li, F., Edwards, J., Candler, G.: Hypersonic boundary layer transition: roughness effects and 3D configurations. NASA Fundamental Aeronautics Program Annual Meeting, Atlanta, GA, October 5–7 (2008)
45. Berger, K., Rufer, S., Kimmel, R., Adamczak, D.: Aerothermodynamic characteristics of boundary layer transition and trip effectiveness of the HIFiRE Flight 5 Vehicle, AIAA Paper 2009-4055 (2009)
46. Choudhari, M., Chang, C.-L., Li, F., Berger, K., Candler, G., Kimmel, R.: Transition analysis for the HIFiRE-5 Vehicle, AIAA Paper 2009-4056 (2009)
47. Kimmel, R.A., Adamczac, D., Juliano, T.: HIFiRE-5 flight test preliminary results, AIAA Paper 2013-0377 (2013)
48. Paredes, P., Theofilis, V.: Centerline instabilities on the hypersonic international flight research experimentation HIFiRE-5 elliptic cone model. J. Fluids Struct. **53**, 36–49 (2015)
49. Juliano, T., Adamczac, D., Kimmel, R.A.: HIFiRE-5 flight test results. J. Spacecr. Rockets **52**, 650–663 (2015)
50. Juliano, T., Borg, M., Schneider, S.P.: Quiet tunnel measurements of HIFiRE-5 boundary-layer transition. AIAA J. **53**, 832–84 (2015)
51. Borg, M., Kimmel, R.A., Stanfield, S.: Traveling crossflow instability for the HIFiRE-5 elliptic cone. J. Spacecr. Rockets **52**, 664–673 (2015)
52. Borg, M.P., Kimmel, R.L.: Ground test of transition for HIFiRE-5b at flight-relevant attitudes. J. Spacecr. Rocket. **55**, 1329–1340 (2018)
53. Neal, I., Leidy, A., Tichenor, N. R., Bowersox, R.: Characterization of environmental disturbances on hypersonic crossflow instability on the HIFiRE-5 Elliptic Cone, AIAA Paper 2018-5375 (2018)
54. Tufts, M.P., Gosse, R., Kimmel, R.L.: PSE analysis of crossflow instability on HIFiRE-5b flight test, AIAA paper 2017-0764 (2017)
55. Kimmel, R.L., Adamczac, D.W., Borg, M.P., Jewell, J.S., Juliano, T.J., Stanfield, S., Tufts, M.P.: HIFiRE-1 and -5 flight and ground tests, AIAA Paper 2018-0056 (2018)
56. Choudhari, M., Li, F., Paredes, P.: Streak instabilities on HIFiRE-5 elliptic cone, AIAA Paper 2020-0828 (2020)
57. Xu, G., Chen, J., Dong, S., Fu, S.: The secondary instabilities of stationary cross-flow vortices in a Mach 6 Swept wing flow. J. Fluid Mech. **873**, 914–941 (2019)
58. Chen, J., Dong, S., Chen, X., Yuan, X., Xu, G.: Stationary cross-flow breakdown in a Swept-Wing boundary layer at Mach 6. Phys. Fluids **33**, 0241808 (2021)
59. Choudhari, M., Li, F., Paredes, P., Duan, L., Computations of crossflow instability in hypersonic boundary layers, AIAA Paper 2017-4300 (2017)
60. Choudhari, M., Li, F., Paredes, P., and Duan, L.: Nonlinear evolution and breakdown of azimuthally compact crossflow vortex pattern over a Yawed Cone, AIAA Paper 2018-1823 (2018)
61. Choudhari, M., Li, F., Paredes, P.: Influence of stationary crossflow modulation on secondary instability, AIAA Paper 2016-3788 (2016)

62. vulcan-cfd.larc.nasa.gov (Last Accessed October 17, 2016)
63. van Albada, G.D., van Leer, B., Roberts, W.W.: A comparative study of computational methods in cosmic gas dynamics. Astron. Astrophys. **108**, 76–84 (1982)
64. Edwards, J.R.: A low-diffusion flux-splitting scheme for Navier-Stokes calculations. Comput. Fluids **6**, 635–659 (1997)
65. Litton, D., Edwards, J., White, J.: Algorithmic enhancements to the VULCAN Navier-Stokes Solver, AIAA Paper 2003–3979 (2003)
66. Cheatwood, F.M., Gnoffo, P.A.: User's manual for the langley aerothermodynamic upwind relaxation algorithm (LAURA), NASA TP 4674 (1996)
67. Choudhari, M.: Roughness-induced generation of crossflow vortices in three-dimensional boundary layers. Theory. ComputFluid Dyn. **6**, 1–30 (1994)
68. Wu, M., Martin, M.P.: Direct numerical simulation of supersonic boundary layer over a compression Ramp. AIAA J. **45**(4), 879–889 (2007)
69. Jiang, G.S., Shu, C.W.: Efficient implementation of weighted ENO schemes. J. Comput. Phys. **126**(1), 202–228 (1996)
70. Williamson, J.: Low-storage Runge-Kutta schemes. J. Comput. Phys. **35**(1), 48–56 (1980)
71. Zhang, C., Duan, L., Choudhari, M.: Direct numerical simulation database for supersonic and hypersonic turbulent boundary layers. AIAA J. **56**, 4297–4311 (2018)
72. Duan, L., Beekman, I., Martin, M.P.: Direct numerical simulation of hypersonic turbulent boundary layers. Part 3: effect of Mach number. J. Fluid. Mech. **672**, 245–267 (2011)
73. Duan, L., Choudhari, M., Li, F.: Direct numerical simulation of crossflow-induced transition in a swept wing boundary layer, AIAA Paper 2013-2617 (2013)
74. Choudhari, M., Li, F., Duan, L., Carpenter, M.H., Streett, C.L., Malik, M.R.: Towards bridging the gaps in holistic transition prediction via numerical simulations, AIAA Paper 2013–2718 (2013)
75. Li, F., Choudhari, M., Spatially developing secondary instabilities and attachment line instability in supersonic boundary layers, AIAA Paper, pp. 2008–590 (2008)
76. Li, F., Choudhari, M.: Spatially developing secondary instabilities in compressible swept airfoil boundary layers. Theoret. Comput. Fluid Dyn. **25**, 65–84 (2011)
77. Paredes, P.: Advances in global instability computations: from incompressible to hypersonic flow. PhD thesis, Technical University of Madrid (2014). http://oa.upm.es/29171/1/Pedro_Paredes_Gonzalez.pdf
78. Paredes, P., Hanifi, A., Theofilis, V., Henningson, D.: The nonlinear PSE-3D concept for transition prediction in flows with a single slowly-varying spatial direction. Procedia IUTAM **14C**, 35–44 (2015)
79. Paredes, P., Choudhari, M., Li, F.: Instability wave-streak interactions in a supersonic boundary layer. J. Fluid Mech. **831**, 524–553 (2017)
80. Saad, Y.: Variations of Arnoldi's method for computing eigenelements of large unsymmetric matrices. Linear Algebra Appl. **34**, 269–295 (1980)
81. Theofilis, V.: Advances in global linear instability of nonparallel and three-dimensional flows. Prog. Aero. Sci. **39**(4), 249–315 (2003)
82. Canuto, C., Hussaini, M., Quarteroni, A., Zang, T.: Spectral Methods. Springer, Berlin (1988)
83. Choudhari, M., Chang, C.-L., Jiang, L.: Towards transition modeling for supersonic laminar flow control. Philos. Trans. R. Soc. Lond. (Phys. Math. Sci.) **363**(1830), 1079–1096 (2005)